

Title No. 121-S65

# Strength and Serviceability of Shear-Critical Post-Tensioned Girders

by Sangyoung Han, Jarrod Zaborac, Jongkwon Choi, Anca C. Ferche, and Oguzhan Bayrak

The results of an experimental program conducted to evaluate the performance of shear-critical post-tensioned I-girders with grouted and ungrouted ducts are presented. The experimental program involved the design, construction, and testing to failure of six full-scale specimens with different duct layouts (straight, parabolic, or hybrid) and using both grouted or ungrouted ducts. All tests resulted in similar failure modes, such as localized web crushing in the vicinity of the duct, regardless of the duct condition or layout. Furthermore, the normalized shear stresses at ultimate were similar for the grouted and ungrouted specimens. The current shear design provisions in the AASHTO LRFD Bridge Design Specifications (AASHTO LRFD) were reviewed, and updated shear-strength reduction factors to account for the presence of the duct in the web and its condition (that is, grouted or ungrouted) were proposed. The data generated from these tests served as the foundation for updated shear-strength reduction factors proposed for implementation in AASHTO LRFD.

**Keywords:** AASHTO LRFD; flexible filler; post-tensioned concrete member; post-tensioning; prestressed I-girder; shear; spliced precast girder.

## INTRODUCTION

Spliced post-tensioned girder technology emerged as a powerful construction application in the United States in the 1970s.<sup>1,2</sup> This construction process has several advantages, including faster construction and the ability to achieve bridge spans of approximately 300 ft (91 m), surpassing the limitations of traditional approaches limited to 170 ft (52 m) due to transportation constraints such as weight and length restrictions.<sup>3</sup> When spliced girders with multistrand post-tensioning systems (that is, post-tensioning tendons) are used, the post-tensioning ducts are injected with a cement-based mixture as the primary choice for corrosion protection, referred to as grouted duct hereafter.<sup>2</sup>

Multistrand post-tensioning systems have traditionally employed cementitious grout to fill the duct to protect the tendons against corrosion and, for bonded post-tensioning, to facilitate the transfer of force between the tendon and the surrounding concrete. The quality of the grout is vital to the tendon performance and durability—any compromise results in significant and accelerated deterioration. Although recently, grout quality has improved significantly, inspection and long-term quality assurance of tendons embedded in grout continue to be challenging, and corrosion issues have been reported.<sup>3</sup> More importantly, the bond between the tendon and the grout makes it significantly difficult to replace potentially damaged tendons. This led to the interest in post-tensioned concrete girders that use flexible fillers in lieu of cementitious grout to fill the post-tensioning ducts, referred to as ungrouted duct hereafter. Hamilton

et al.<sup>4</sup> evaluated the constructability of ungrouted duct systems using non-cementitious flexible filler materials, such as petroleum wax, grease, and gel, and successfully demonstrated viable options for the replacement of the grout mixture. The use of flexible fillers can overcome the innate problem of grout quality and ease prospective tendon replacement procedures. To this end, a non-cementitious material to fill the post-tensioning duct has been adopted by the Florida Department of Transportation.<sup>3</sup>

Design applications for spliced girders have been embodied in various code provisions, such as the AASHTO general procedure,<sup>5</sup> AASHTO segmental procedure,<sup>6</sup> PCI Bridge Design Manual,<sup>7</sup> Eurocode 2<sup>8</sup>, and *fib* Model Code.<sup>9</sup> Invariably, for the calculation of the shear capacity, the aforementioned provisions apply a web-width reduction factor ( $k$ ), intended to account for the effect of the post-tensioning duct on the shear strength. As summarized in Table 1, the design provisions adopt different values for the web-width reduction factor. The most recent edition of the AASHTO general procedure for shear design (hereafter referred to as AASHTO LRFD), includes a web-width reduction factor, in addition to the novel inclusion of a shear-strength reduction factor ( $\lambda_{duct}$ ). To assess the adequacy of the AASHTO LRFD reduction factors ( $k$  and  $\lambda_{duct}$ ), Moore et al.<sup>10</sup> conducted tests on large-scale post-tensioned members with grouted ducts only. As a result, the AASHTO LRFD provisions were verified against an incomplete database of specimens and could result in potentially inadequately designed

**Table 1—Web-width reduction factors for codes considered**

Code provision	Ungrouted steel duct	Grouted steel duct	Ungrouted plastic duct	Grouted plastic duct
AASHTO general procedure <sup>5</sup>	1.0	0.0	1.0	0.0
AASHTO segmental procedure <sup>6</sup>	1.0	0.5	1.0	0.5
PCI Bridge Design Manual <sup>7</sup>	0.5	0.25	0.5	0.25
Eurocode 2 <sup>8</sup>	1.2	0.5	1.2	1.2
<i>fib</i> Model Code <sup>9</sup>	1.2	0.5	1.2	0.8

*ACI Structural Journal*, V. 121, No. 5, September 2024.

MS No. S-2022-398.R4, doi: 10.14359/51740847, received March 27, 2024, and reviewed under Institute publication policies. Copyright © 2024, American Concrete Institute. All rights reserved, including the making of copies unless permission is obtained from the copyright proprietors. Pertinent discussion including author's closure, if any, will be published ten months from this journal's date if the discussion is received within four months of the paper's print publication.

post-tensioned girders with the ungrouted ducts. Thus, large-scale testing was necessary to investigate the response of ungrouted post-tensioned specimens.

The work presented herein was conducted to advance the knowledge of the response of shear-critical post-tensioned girders with ungrouted ducts and address the lack of large-scale experimental data on the response of this type of structural member. A thorough experimental program was designed to compare the structural performance of girders with different post-tensioning profiles and either grouted or ungrouted ducts. The experimental program focused on two main variables: 1) three different duct layouts (that is, straight, parabolic, and hybrid); and 2) grouted and ungrouted ducts for each layout. As the contribution of flexible fillers to the shear behavior is negligible, it was assumed that the shear performance of post-tensioning girders with flexible fillers would be similar to those with empty ungrouted ducts.<sup>11</sup> Despite its extensive scope, the testing program did not aim to incorporate every conceivable design variable. Instead, it prioritized the most influential ones to significantly enhance the knowledge and comprehension of the behavior of shear-critical post-tensioned girders with grouted and ungrouted ducts.

The experimental program comprised three key components: 1) fabrication of six test specimens in a precast plant, ensuring consistent fabrication practices with those employed for precast bridge elements; 2) conducting 12 full-scale laboratory tests on the girders to study the shear behavior; and 3) analyzing the structural response data. As a result of this research, modifications were suggested to enhance the calculation of shear resistance in the AASHTO LRFD general procedure of post-tensioned members. These advancements contribute to a better understanding of the shear response in post-tensioned concrete members and pave the way for improved design practices.

## RESEARCH SIGNIFICANCE

The research significance of this study lies in the growing interest in unbonded multistrand post-tensioning systems using flexible fillers, which address the durability concerns introduced by cementitious grout. Understanding the large-scale behavior of such members, especially in terms of shear performance, is crucial. The primary goal of this research was to enhance the understanding of the response exhibited by shear-critical post-tensioned girders with ungrouted ducts concerning both strength and serviceability. Through an extensive experimental program, direct comparisons were made between the behavior of I-girders with grouted and ungrouted ducts. The findings from testing of large-scale specimens offered valuable insight into the behavior and governing failure mechanisms. This research's meticulous analysis of large-scale test data shed light on the underlying shear-resisting mechanisms of post-tensioned concrete members. Consequently, the research led to proposed modifications for the calculation of shear resistance in the AASHTO LRFD general procedure for shear design. These modifications aim to improve the design practices for post-tensioned concrete girders.

## BACKGROUND: AASHTO LRFD GENERAL SHEAR DESIGN PROVISIONS

The AASHTO LRFD general procedure for sectional shear design is based on the Modified Compression Field Theory (MCFT).<sup>12</sup> A series of simplifying assumptions were made to recast the MCFT into design equations, including: the longitudinal strain is assumed to be distributed linearly over the depth of the member, the orientation of the compressive stress field is unchanged over the depth, and it is assumed the stirrups yield before concrete crushing occurs. These simplifications facilitate the application of the MCFT to practical design scenarios, allowing for the calculation of shear capacity in reinforced and prestressed concrete members in accordance with AASHTO LRFD guidelines.

### Nominal shear resistance in AASHTO LRFD

The nominal shear resistance in AASHTO LRFD<sup>5</sup> is calculated as the lesser of the following two equations

$$V_{n1} = V_c + V_s + V_p \quad (1)$$

$$V_{n2} = 0.25f'_c b_v d_v + V_p \quad (2)$$

Equation (1), referred to as  $V_{n1}$  hereafter, represents the shear resistance provided by the concrete component ( $V_c$ ), the transverse reinforcement ( $V_s$ ), and the component of the prestressing force in the direction of the shear force ( $V_p$ ), which is taken as positive if it is resisting the applied shear. Equation (2), referred to as  $V_{n2}$  hereafter, is an upper limit on the nominal shear resistance intended to ensure that the concrete in the web will not crush prior to the yield of the transverse reinforcement.

The shear resistance contribution of the concrete,  $V_c$ , represents the ability of cracked concrete to carry shear stresses through aggregate interlock action, and it is evaluated as

$$V_c = 0.0316\beta\sqrt{f'_c}b_v d_v \text{ (Imperial units)} \quad (3)$$

The shear resistance provided by the transverse reinforcement,  $V_s$ , is calculated as

$$V_s = \frac{A_s f_y d_v (\cot\theta + \cot\alpha) \sin\alpha}{s} \lambda_{duct} \quad (4)$$

One of the assumptions of the shear design provisions in AASHTO LRFD is that the stirrups shall yield before the concrete fails in compression through web crushing. A study by Bentz et al.<sup>13</sup> derived an ultimate shear stress limit of  $0.25f'_c$  and validated the normalized shear stress to prevent concrete crushing prior to stirrup yielding. This led to the development of Eq. (2) as an upper limit imposed on the nominal shear resistance.

### Effective web-width factor, $b_v$

The reduction in shear resistance due to the presence of ungrouted ducts is taken into account by reducing the web width, as per Article 5.7.2.8 in AASHTO LRFD. The effective web width,  $b_v$ , is calculated as

$$b_v = b_w - k\phi_{duct} \quad (5)$$

For post-tensioned members with ungrouted ducts, the web width is reduced by the diameter of the duct; therefore,  $k$  has a value equal to 1.0. No web-width reduction is applied for grouted ducts; as such,  $k$  has a value equal to 0.0. Originally, the coefficient  $k$  was evaluated based on results obtained from small-scale panel tests, designed to be representative of the diagonal compressive strut formed by shear loading within a beam.<sup>14,15</sup> The coefficient  $k$  was assigned values based on the duct material (corrugated metal or plastic), as well as the duct conditions (grouted or ungrouted). The current values for  $k$  in AASHTO LRFD were derived from large-scale post-tensioned I-girder specimens conducted by Moore et al.<sup>10</sup> that solely considered grouted duct conditions.

### Shear-strength reduction factor, $\lambda_{duct}$

AASHTO LRFD accounts for the reduction in shear resistance due to the presence of grouted ducts through the shear-strength reduction factor,  $\lambda_{duct}$ , introduced in the calculation of the transverse reinforcement contribution,  $V_s$ . The shear-strength reduction factor,  $\lambda_{duct}$ , was derived based on the reduction in the strength of the concrete compressive diagonal strut due to the presence of a post-tensioning duct. The reason behind this approach is rooted in the fact that the transverse reinforcement contribution to the nominal shear strength is limited by the ability of the truss mechanism to resist the shear force demand through both the tensile capacity of the transverse reinforcement and the compressive capacity of the concrete in the web.<sup>10,16</sup>

The discontinuity in the concrete compressive stress field, introduced by the presence of the duct, disrupts the internal force transfer in the assumed truss mechanism between the transverse reinforcement and the concrete compression struts. The detrimental effect of the presence of the duct was expressed through the introduction of  $\lambda_{duct}$  in the calculation of the force developed in the concrete compression strut,  $V_{web}$ , as per Eq. (6)

$$V_{web} = \lambda_{duct} f_2 \cos\theta d_v b_w \quad (6)$$

From equilibrium, the vertical component of the concrete compressive strut is equal to the force developed in the tie, representing the transverse reinforcement, as shown in Eq. (7)

$$(\lambda_{duct} \cdot f_2 \cos\theta d_v b_w) \sin\theta = \frac{A_s f_y d_v \cot\theta}{s} \cdot \lambda_{duct} \quad (7)$$

Thus, the nominal shear resistance,  $V_{n1}$ , can be expressed as per Eq. (8), which is similar to the AASHTO LRFD<sup>5</sup> shear-strength equation when the direction of transverse reinforcement is vertical ( $\alpha = 90$  degrees).

$$\begin{aligned} V_{n1} &= V_c + V_s + V_p \\ &= 0.0316\beta\sqrt{f'_c} b_w d_v + \frac{A_s f_y d_v \cot\theta}{s} \lambda_{duct} + V_p \end{aligned} \quad (8)$$

The factor,  $\lambda_{duct}$ , is calculated as a function of the duct diameter correction factor,  $\delta$ , duct diameter,  $\phi_{duct}$ , and gross web width,  $b_w$ , as shown in Eq. (9)

$$\lambda_{duct} = 1 - \delta \cdot \left( \frac{\phi_{duct}}{b_w} \right)^2 \quad (9)$$

The value of  $\delta$  accounts for whether the duct is grouted or ungrouted. Moore et al.<sup>10</sup> validated the value of  $\delta$  equal to 2.0 for grouted ducts based on the results of their large-scale test. For ungrouted ducts, the value of  $\delta$  was taken as 0.0, as no data were available.

## EXPERIMENTAL INVESTIGATION

### Design of test specimens

In this experimental program, the test specimens were designed using representative construction practices of the Texas Department of Transportation (TxDOT). The specimens were 600 in. (1524 cm) long, 62 in. (158 cm) tall I-girders with an 8 in. (20 cm) thick deck on top. The web width and the duct diameter were selected as 9 and 4 in. (23 and 10 cm), respectively. This section is commonly referred to as the Tx62-Girder. To accommodate post-tensioning anchorages at the end regions of the Tx62-Girder, a typical enlarged end block was employed from the reference design of the Washington State Department of Transportation (WSDOT).<sup>17</sup>

For the precast test specimens, 0.6 in. (1.5 cm) low-relaxation strands were used for the pretensioning. A total of 58 pretensioning strands were provided. Each test specimen contained one or two post-tensioning multistrand systems comprised of nineteen 0.6 in. (1.5 cm) low-relaxation pretensioning strands. Anchorage assemblies and corrugated high-density polyethylene (HDPE) ducts for post-tensioning by VSL International were used as the multistrand post-tensioning system. The overall dimensions of these girders are shown in Fig. 1, and more detailed geometry information is found in Appendix A.\*

The girder specimens were designed with three different post-tensioning duct profiles: one straight duct, one parabolic duct, and a combination of one parabolic and one straight duct, as shown in Fig. 2. More specifically, the first set of specimens, referred to as Tx62-0SG (grouted duct) and Tx62-0SU (ungrouted duct), were fabricated with a straight duct positioned at the midheight of the composite girder. The second set of test specimens, referred to as Tx62-P0G (grouted duct) and Tx62-P0U (ungrouted duct), were fabricated with a parabolic duct to investigate the effect of tendon curvature on sectional stress flow. The last set of fabricated specimens, referred to as Tx62-PSG (grouted duct) and Tx62-PSU (ungrouted duct), had a parabolic duct at the same location as the second set and one additional straight duct at the intersection between the web and bottom flange. The locations of couplers, shown in Fig. 2, were selected to avoid any undesired influence that the larger-diameter

\*The Appendix is available at [www.concrete.org/publications](http://www.concrete.org/publications) in PDF format, appended to the online version of the published paper. It is also available in hard copy from ACI headquarters for a fee equal to the cost of reproduction plus handling at the time of the request.



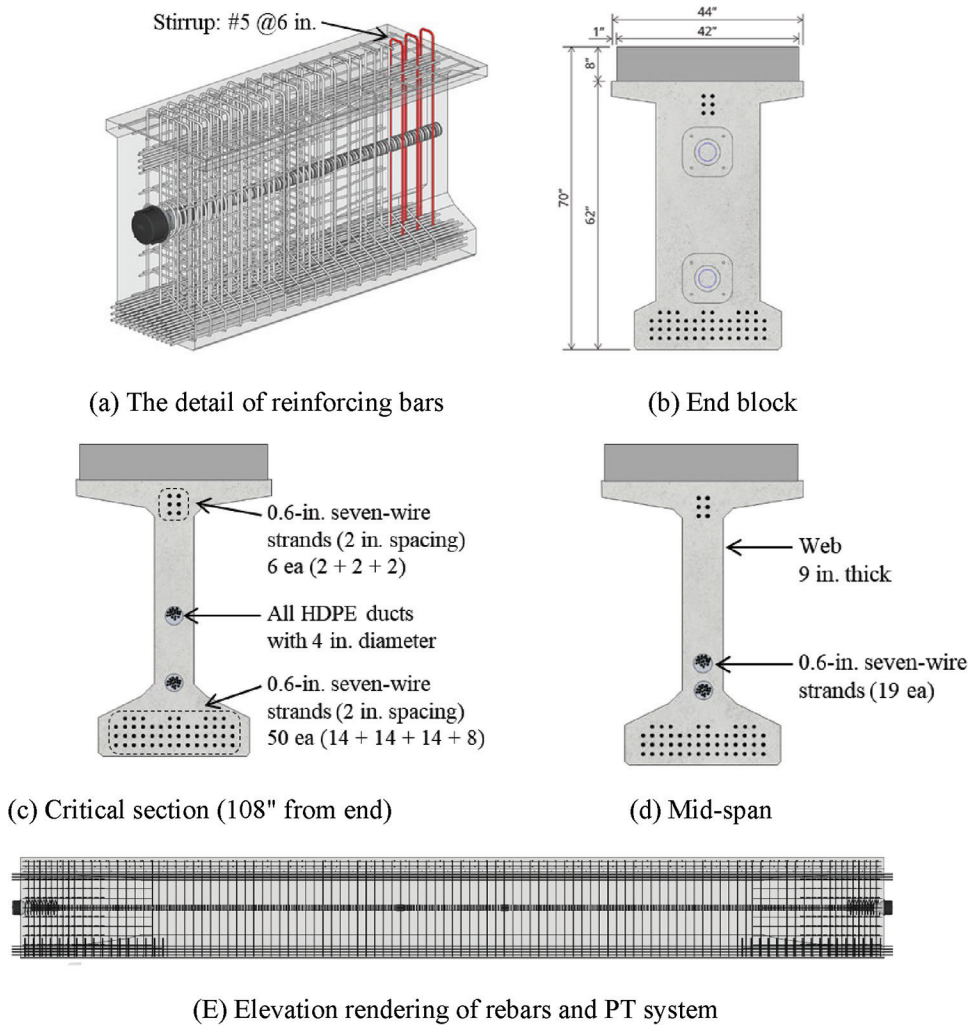


Fig. 1—Details of reinforcing bars and cross sections of test specimens of Tx62-PSG and Tx62-PSU. (Note: 1 in. = 25.4 mm.)

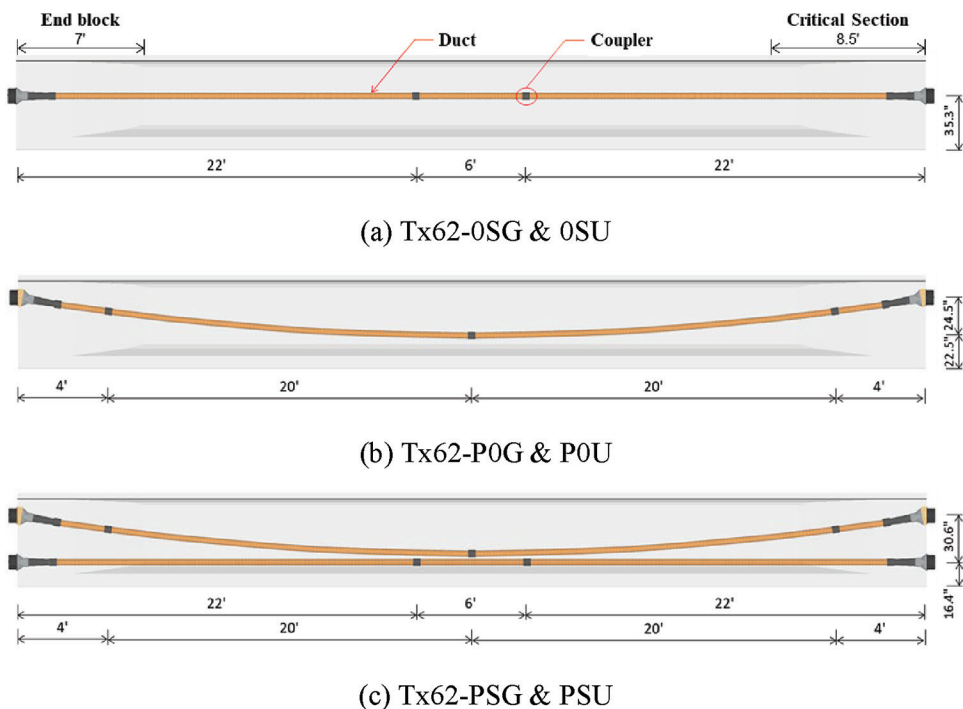
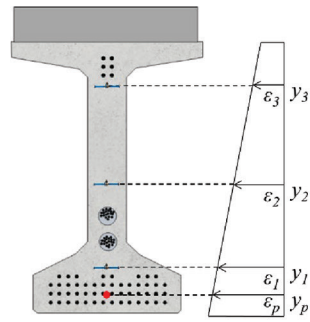
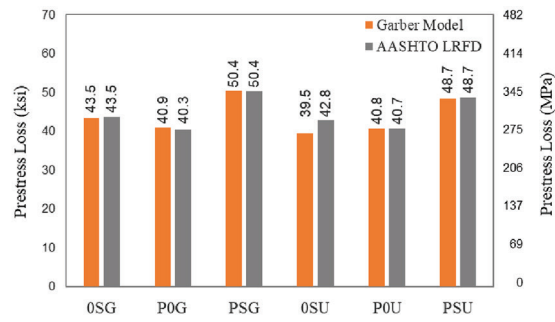


Fig. 2—Duct layout with location of couplers. (Note: 1 in. = 25.4 mm; 1 ft = 304.8 mm.)





(a) Garber Model by internal distribution



(b) Determined prestress loss

Fig. 3—Prestress loss of test specimen to determine shear strength.

duct coupler could have on the shear performance within the test region.

### Test specimen fabrication

The specimens were fabricated at a local precast plant, Valley Prestress Products, Inc. (VPP) in Eagle Lake, TX, thereby ensuring fabrication practices are consistent with those used for precast bridge elements. The process of pretensioning was conducted up to the design prestress level of 202 ksi (1393 MPa) according to the limiting stress of  $0.75f_{pu}$ .<sup>5</sup> The actual observed prestress was 206 ksi (1420 MPa), within the acceptable tolerance of  $\pm 5\%$ .<sup>18</sup> Finally, the work process of the individual strand prestressing release was conducted for all test specimens, after checking that the cylinder compressive strength of 10.1 ksi (69.6 MPa),  $f_{ci}'$ , was greater than the design strength of 7.5 ksi (52 MPa).<sup>18</sup> After the fabrication of precast girders from the local plant, the test specimens were transferred to the Ferguson Structural Engineering Laboratory (FSEL) at The University of Texas at Austin, where a specialized post-tensioning operating company, Structural Technologies in Dallas, TX, performed the post-tensioning and grouting. Similar to the pretensioning, the stress level of post-tensioning was conducted up to the design prestress level of 202 ksi (1393 MPa). To better predict the structural behavior of post-tensioned members, it is imperative to quantify the time-dependent prestress loss in the tendon. Garber et al.<sup>19</sup> developed a novel method for prestress loss estimation using the internal strain distribution. This method, using data from embedded strain gauges, calculates the prestress loss at events such as prestress transfer, post-tensioning, and deck casting. Figure 3 illustrates the prestress loss at different stages before testing, comparing the Garber model<sup>19</sup> with AASHTO LRFD. The research report by Han et al.<sup>20</sup> provides further details on the fabrication process of the specimens, including the pretensioning, post-tensioning, precast, and cast-in-place concrete casting.

### Material properties

A self-consolidating concrete (SCC) mixture was used to cast the specimens, consistent with standard practice for the construction of Tx-girders. All girders were cast with the same concrete mixture supplied by the VPP batch plants. The concrete mixture design used is provided in Table 2. Standard cylindrical concrete samples accompanying

Table 2—Concrete mixture design

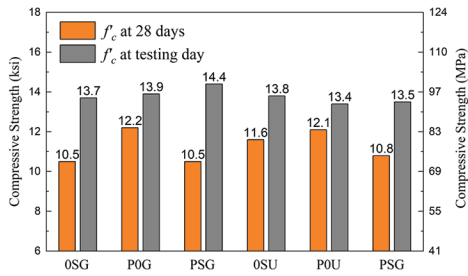
Material	Detail	Amount	Units	
Cementitious material	Type III cement	600 (356)	lb/yd <sup>3</sup> (kg/m <sup>3</sup> )	
	Class F fly ash	150 (89)		
Fine aggregate	Sand (fineness modulus = 2.88)	1266 (751)		
Coarse aggregate	Natural gravel (3/4 in. nominal maximum)	1733 (1028)		
Water	Water	235 (139)		
	w/cm	0.34		
Admixtures	High-range water-reducing admixture	7.0 (456)		oz./100 lb cementitious materials (mL/100 kg)
	Water reducer/retarder	1.0 (65)		
	Corrosion inhibitor	51.0 (3325)		
	Viscosity modifier	3.5 (228)		

Note: w/cm is water-cementitious materials ratio.

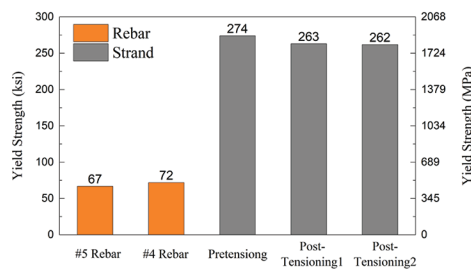
each test specimen (a total number of 120 samples for six girders) were cast for compression tests at prestressing release, 28 days after casting, post-tensioning, and structural testing. Figure 4(a) shows the compression test results<sup>21</sup> at 28 days and on the structural test day. In addition, tensile tests were performed on the nonprestressed reinforcing bars and the 0.6 in. (1.5 cm) seven-wire strands (low-relaxation). Note that the design of transverse reinforcement in the general section consisted of No. 5 double-stirrup deformed reinforcing bar (0.625 in. [15.875 mm]) with the uniform spacing of 6 in. (152 mm) along the length of girder (reinforcement ratio of 1.15%). Figure 4(b) shows the average yield strength of three samples that satisfied the ASTM standards for reinforcing bars<sup>22</sup> (67 ksi [462 MPa] for No. 5 and 72 ksi [496 MPa] for No. 4) and 0.6 in. (1.5 cm) seven-wire strands<sup>23</sup> (274 ksi [1889 MPa] for pretensioning and 262.5 ksi [1810 MPa] for post-tensioning), respectively. The measured material properties were used to calculate the nominal shear resistance using AASHTO LRFD.

### Structural test configuration and protocol

In this experimental program, six test specimens were fabricated, and 12 shear tests were conducted. The failure load was estimated using the AASHTO LRFD<sup>5</sup> shear provision to be less than 1800 kip (8000 kN). A 20% reserve

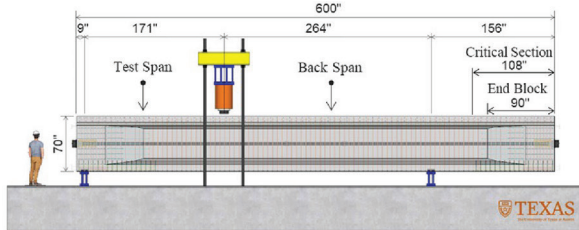


(a) Compressive test results of concrete

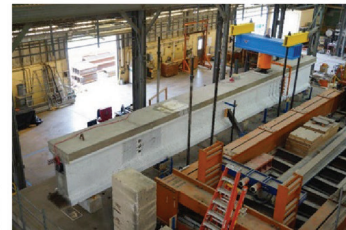


(b) Yield strength of reinforcing bars

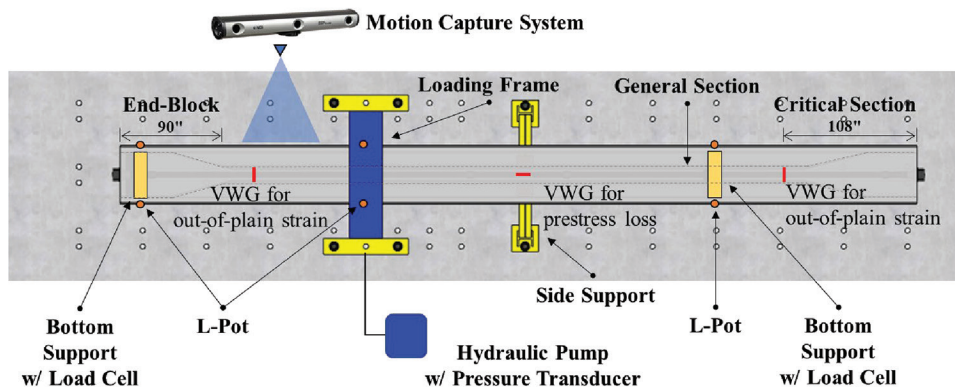
Fig. 4—Results of material tests. (Note: 1 ksi = 6.9 MPa.)



(a) Elevation for the shear structural test



(b) Structural setup with test specimen



(c) Plan for the instrumentation setup along with the test specimen

Fig. 5—Design and rendering of shear structural test schematic. (Note: 1 in. = 25.4 mm.)

capacity was provided to the test setup to account for potential overstrength. Thus, the test frame was designed for 2000 kip (8900 kN). The strength of the loading frame was verified by its calculated resistance using an American Institute of Steel Construction (AISC) provision in terms of sectional flexural capacity, sectional shear capacity, and welding strength.<sup>24</sup> Figure 5 shows the structural setup and monitoring area designed for this study. Two tests were conducted on each of the six specimens. The load was applied monotonically until shear failure occurred. The load was applied in 50 kip (222 kN) increments until the first diagonal shear crack detection. After crack detection, the loading was applied in 75 kip (333 kN) increments. The loading was paused to measure and map cracks up until the critical shear crack developed. The loading was then increased until the test specimen experienced failure. After failure, the applied load was removed, and a final cracking survey was performed.

AASHTO LRFD takes the location of the critical shear section for the girder, determined as the effective shear depth ( $d_v$ ) from the edge of the bearing pad (65 in. [165 cm]);

however, this is located within the end block (the general beam section starts 90 in. [229 cm] from the end). A more practical approach to determining the critical section relates to the failure cracks, based on a visual inspection of Moore et al.'s test results,<sup>10</sup> because the geometric condition of test specimens is precisely replicated. The most vulnerable area for shear force was reported to be approximately 18 in. (46 cm) from the termination of the end block, defined as the critical section for this experimental study. This determined critical section of the test specimen serves as the critical location for the calculation of shear force and the various instrumentation applied to the specimens. In conclusion, the experimentally determined critical section from Moore et al.<sup>10</sup> is reasonably close to the location of the governed failure crack in this study.

## EXPERIMENTAL RESULTS AND DISCUSSION

### Failure mechanism

All girders behaved and failed in a similar manner. First, hairline cracks were observed at the duct location,

which further developed along the length of the girder as the applied load increased. At approximately 80% of the ultimate load, a dominant shear crack developed from the center of the web to the top and bottom flanges in the test span. Note that this study conducted the stiffness analysis and determined the specimen's change point from linear to nonlinear behavior (details are provided in Appendix B). This change point coincided with the onset of a fully developed diagonal shear crack, consistently occurring at load levels of approximately 80% of the ultimate load. Finally, the test specimens failed due to concrete compression failure in the vicinity of the post-tensioning duct, a result otherwise known as web crushing.

Cracking development and ultimate failure mode were consistent in the grouted and ungrouted post-tensioning ducts. Figure 6 illustrates the three different cracking modes related to load and deflection. In addition, Fig. 7 shows load-deflection plots and failure crack patterns for all 12 tests. Given that a direct comparison of the ultimate shear capacity across specimens may be compromised in the absence of normalization, the subsequent discussion will focus on elucidating the ultimate behavior within the context of the "Ultimate level" section. With respect to the diagonal cracking propagation, each specimen containing the same profile of post-tensioning duct experienced a similar cracking pattern, with an average crack spacing recorded between 6.5 and 7.0 in. (16.5 and 17.8 cm)—a finding closely paralleling the 6.4 in. (16.3 cm) computed by Collins and Mitchell.<sup>2</sup> Moreover, the inclination of the diagonal cracks ranged from 26 to 30 degrees, aligning closely with approximately 29 degrees as determined by the AASHTO LRFD.<sup>5</sup>

After testing, the specimens were cut with a wire saw at the critical section as an additional visual inspection to further analyze the cross-sectional behavior and identify potential particularities specific to specimens containing grouted or ungrouted ducts. Figure 8 shows the visual inspection for the developed cracking patterns, such as diagonal shear crack, localized web crushing, and splitting cracks. More importantly, the internal cracking survey revealed the splitting cracks that developed around the duct. This splitting cracking behavior was the result of the splitting stresses in the vicinity of the duct; the embedded vibrating-wire gauges (VWGs) quantified this behavior.

## Web behavior in out-of-plane direction

The presence of post-tensioning ducts in the web region of a Tx62 girder introduces a sectional discontinuity that influences the stress distribution around the duct and affects the shear behavior and capacity of the girder. Figure 9 depicts the early studies that addressed the phenomenon and shows a deviation in the compressive stress flow in the vicinity of a post-tensioning duct.<sup>25</sup> The through-thickness tensile stresses develop where the compressive stresses start to deviate toward the grouted duct area because the grout was assumed to be typically stiffer than the surrounding concrete. However, in a section with an empty duct, the compressive stresses flow around the empty duct and through-thickness tensile stresses develop in the immediate vicinity of the duct. In both cases, through-thickness tensile stresses are induced by the deviation in compressive stresses, which resulted in a reduction in the shear capacity of the member.<sup>14,16</sup>

The previous study on the panel-based analogy did not include an investigation of the actual structural boundary conditions.<sup>14,15</sup> Moore et al.<sup>10</sup> pointed out that the contrasting results between the panel-based tests and the large-scale tests were primarily due to different governing failure mechanisms. Specifically, all panel-based tests conducted by Wald et al.<sup>15</sup> reported splitting failure in the out-of-plane direction, which resulted from the compressive-controlled boundary condition. This test setup is unlikely to accurately simulate the shear mechanism that develops in structural members, such as an I-girder, and leads to a governed splitting failure, similar to concrete tests assessing splitting tensile strength.<sup>26</sup> Therefore, caution should be exercised when extrapolating findings from panel-based tests to understand the shear performance of complex structural members such as I-girders. Large-scale tests on actual structural elements are essential for obtaining accurate and reliable data on their shear behavior.

In this study, a series of VWGs were strategically placed in the vicinity of ducts to measure out-of-plane strains during the structural test. Depending on the duct profile, either four or six VWGs were embedded. Table 3 presents the measured tensile strain at each location during the test. Notably, in the region around the duct area, the VWG recorded increasing tensile strains in the out-of-plane direction. To evaluate tensile strain levels in the out-of-plane direction, three stages were selected: 1) prior to the development of the first hairline shear crack; 2) at the point of initiating nonlinearity in the

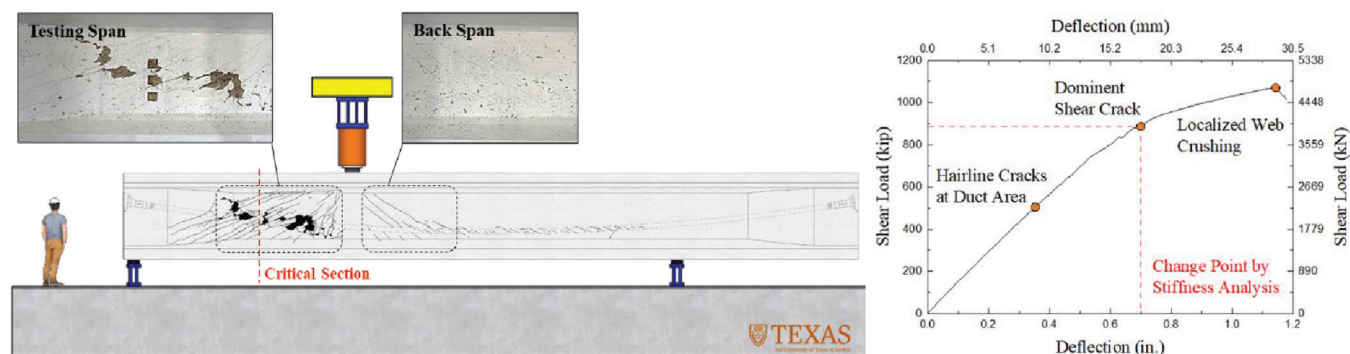


Fig. 6—Structural setup and three distinct cracking modes related to loading and deflection.



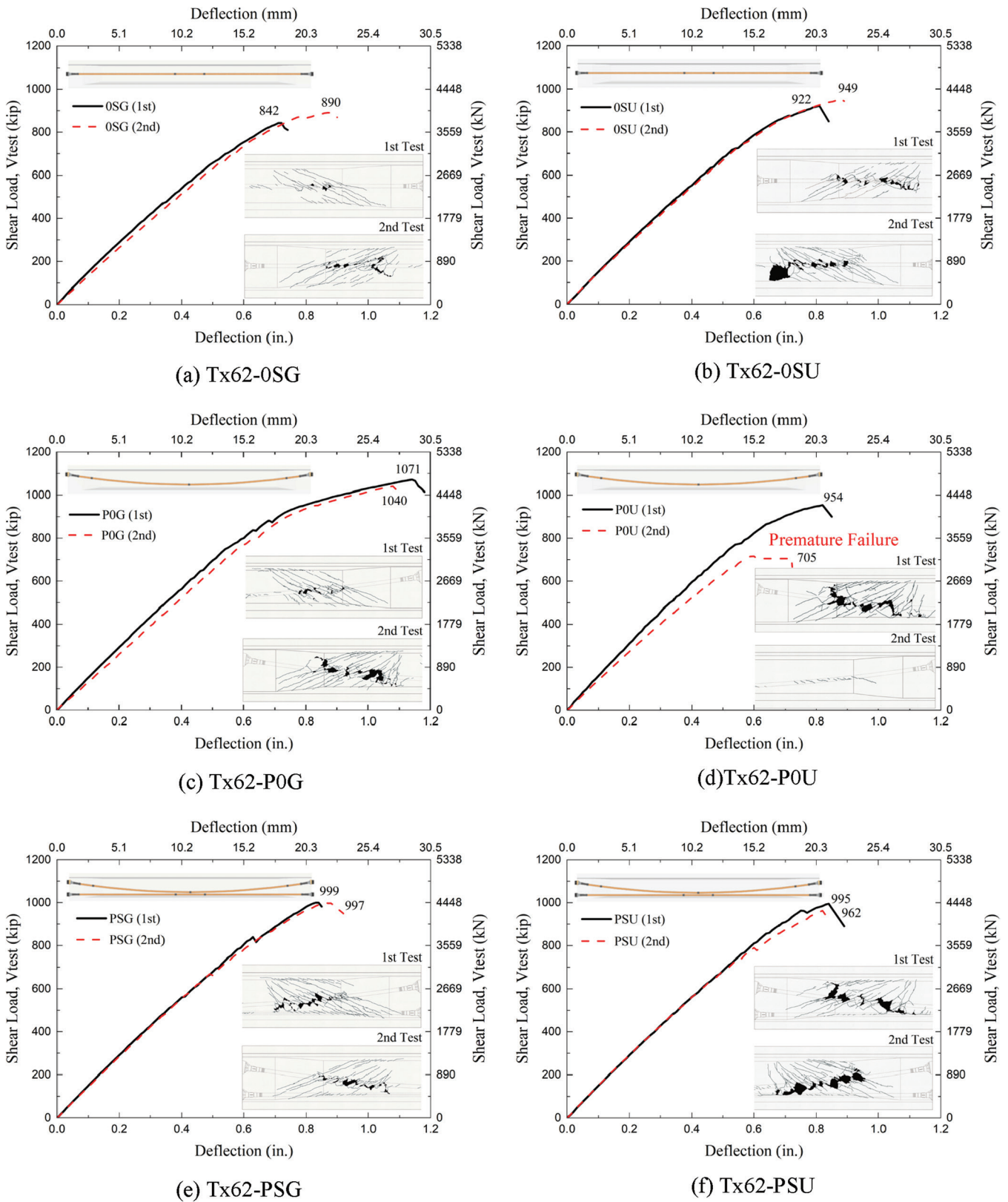


Fig. 7—Shear load-deflection plots of all test specimens with surface cracks.

behavior; and 3) at the level of ultimate load. Following the initiation of nonlinearity, a noticeable escalation in tensile strains was observed, although the intensity of these tensile strains exhibited a certain degree of variation. Of particular significance, two locations near the duct at the middle of the web height (referred to as Mid 1 and Mid 2) exhibited

substantial expansion in the out-of-plane direction regardless of duct condition. This observation contradicts the findings of the study on the panel-based analogy,<sup>14,15</sup> as shown in Fig. 9.<sup>25</sup> The discrepancy suggests that the shear behavior and failure mechanism in these structural members, particularly

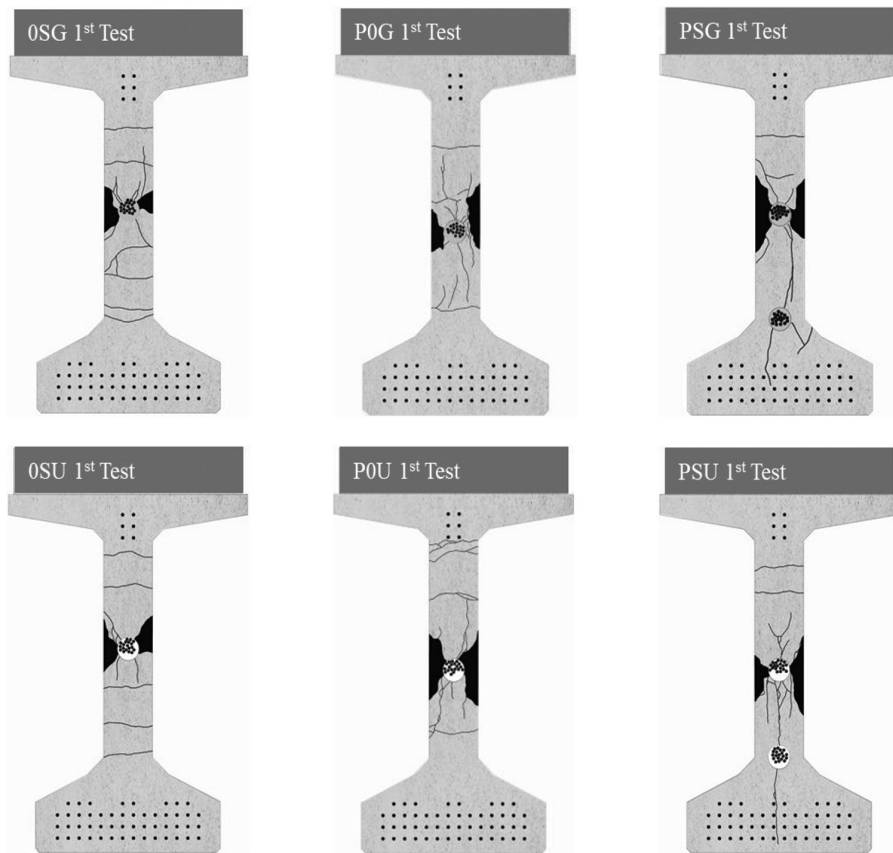


Fig. 8—Internal cracking survey at critical section.

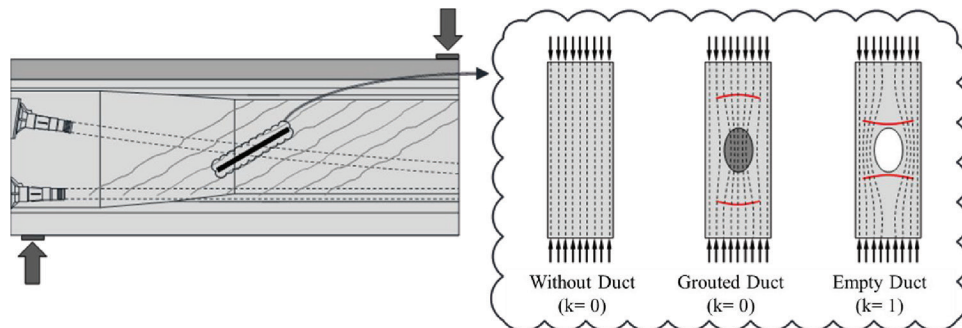


Fig. 9—Internal compressive stress flow in web of post-tensioned girder and concrete panel analogy of specimens without duct, grouted duct, and empty duct.<sup>25</sup>

in the vicinity of ducts, differ significantly from what the panel-based analogy previously indicated.

### Web behavior in in-plane direction

In addition to measuring physical displacements, this study monitored the strains during the structural test using a motion-capture system. This motion-capture system tracks the position of infrared light-emitting diodes referred to as markers. These data were post-processed and used to investigate the web area's strain distribution, which aided in identifying the controlled failure mechanism over the course of the structural test. For this study, the markers were installed to form a 6 in. (152 mm) grid within the test region. The recorded displacements of the markers were used to estimate the average strain of each 6 x 6 in. (152 x 152 mm) quadrilateral element. Note that data were only collected

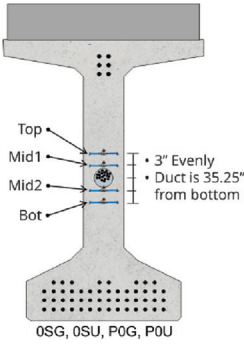
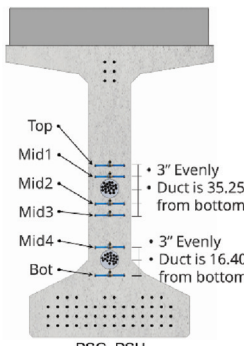
for four specimens—Tx62-0SG, 0SU, P0G, and PSU—due to an unexpected instrumentation malfunction for specimens Tx62-P0U and PSG. Thus, this paper will discuss the available motion-capture data from Tx-0SG, 0SU, P0G, and PSU only.

In post-processing, the data collected from the markers was subdivided from the quadrilateral elements defined by four markers into two triangles, each defined by three markers. The shape functions from constant strain triangle elements estimate the strain based on the nodal displacements. Finally, an area-weighted average of the two triangles determines the average strain in the quadrilateral region.

### Service-level cracking

The serviceability of structural components and their structural performance at the service level of loading are

**Table 3—Web expansion at critical section determined by VWGs**

Measurement location	ID	Shear load, kip (kN)	Top, $\mu\epsilon$	Mid 1, $\mu\epsilon$	Mid 2, $\mu\epsilon$	Mid 3, $\mu\epsilon$	Mid 4, $\mu\epsilon$	Bottom, $\mu\epsilon$
 <p>OSG, OSU, POG, POU</p>	OSG	600 (2669) <sup>†</sup>	6	43	38	—	—	-11
		722 (3212) <sup>‡</sup>	16	200	223	—	—	-8
		842 (3746) <sup>§</sup>	18	450	459	—	—	4
	POG	600 (2669) <sup>†</sup>	-1	25	42	—	—	-21
		888 (3950) <sup>‡</sup>	1223	1781	1489	—	—	347
		1071 (4764) <sup>§</sup>	OR*	OR*	OR*	—	—	OR*
	PSG	600 (2669) <sup>†</sup>	5	42	41	-18	-25	-33
		751 (3340) <sup>‡</sup>	16	799	862	-12	-27	-13
		998 (4437) <sup>§</sup>	OR*	OR*	OR*	1682	127	4
 <p>OSU, PSU</p>	OSU	600 (2669) <sup>†</sup>	10	197	48	—	—	-12
		739 (3289) <sup>‡</sup>	26	758	353	—	—	-10
		918 (4083) <sup>§</sup>	849	OR*	OR*	—	—	1646
	POU	600 (2669) <sup>†</sup>	2	35	91	—	—	-22
		823 (3662) <sup>‡</sup>	45	1025	OR*	—	—	341
		955 (4247) <sup>§</sup>	1066	OR*	OR*	—	—	2061
	PSU	600 (2669) <sup>†</sup>	-3	43	63	-25	-29	-43
		843 (3751) <sup>‡</sup>	23	622	424	-21	-5	-23
		995 (4424) <sup>§</sup>	OR*	OR*	OR*	OR*	55	-18

\*OR (out-of-range) indicates that tensile strain in out-of-plane direction exceeded gauge's measurement range.

<sup>†</sup>Specimen statement subjected to in-plane shear loading before shear crack.

<sup>‡</sup>Specimen statement subjected to in-plane shear loading starting nonlinear.

<sup>§</sup>Specimen statement subjected to in-plane shear loading ultimate failure.

considered in the aspects of cracking, deformation, and concrete stresses according to AASHTO LRFD.<sup>5</sup> The current version of ACI 318<sup>27</sup> removed the crack-width-based limitation to define the serviceability. However, ACI 224R-01<sup>28</sup> and the *fib* Model Code<sup>9</sup> continue to use the crack width as a metric for serviceability. Based on the notion of determining the serviceability using the crack width criteria, an early study by Birrcher et al.<sup>29</sup> provided an experimental-based methodology to determine the serviceability performance of elements subjected to in-plane shear loading. The Birrcher model adopts the ratio of the shear-resistance factor ( $\phi$ ) to the load factor ( $\eta$ ), which is approximately equal to the ratio of the service-level load to the nominal capacity. The ratio of service-level load to nominal capacity is determined as

$$\phi \cdot \text{Nominal Capacity} = \eta \cdot \text{Service-Level Load} \quad (10)$$

where  $\phi$  is the shear-resistance factor of 0.75; and  $\eta$  is the load factor defined as a function of the load case and the distribution of the loads.

This study uses the suggested  $\eta$  factor equal to 1.4 based on the assumptions of: 1) Strength I—basic load combination relating to the normal vehicular use of the bridge without wind—in AASHTO LRFD<sup>5</sup> governs design, 1.25 dead load

(DL) + 1.75 live load (LL); and 2) 75% of the service load is DL and 25% of the service load is LL.

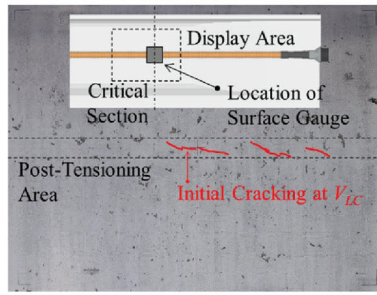
Using Eq. (10), Birrcher et al.<sup>29</sup> reported the proposed model to compute the ratio of service-level load to experimental capacity can be calculated as

$$\frac{V_n}{V_{test}} \cdot \frac{\phi}{\eta} = \frac{1}{1.3} \cdot \frac{0.9}{1.4} = 0.5 \quad (11)$$

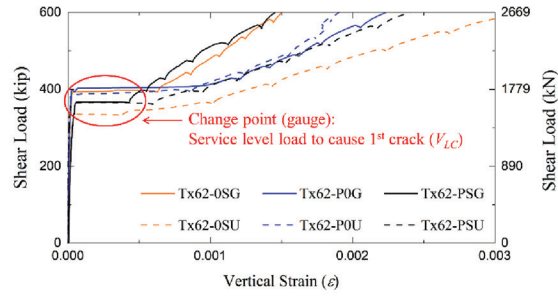
where  $V_n$  is the nominal shear resistance; and  $V_{test}$  is the shear strength from the test. In this study, the ratio of the nominal shear resistance to ultimate strength equals 1.3. The computed ratio of approximately 0.5, which is related to the relationship between the experimental ultimate shear capacity and the nominal capacity of a section, is the service-level load as a function of  $V_{test}$  for this study.

This study reviews Birrcher et al.'s approach to determine the serviceability of post-tensioned concrete members. The service load is compared with the measured shear load that caused the first cracking (referred to as  $V_{LC}$ ) to evaluate the serviceability of the specimens. All post-tensioned test specimens, regardless of duct conditions, experienced initial hairline cracks in the duct area, as shown in Fig. 10(a), which occurred at a shear-force level of  $V_{LC}$ . To refine the



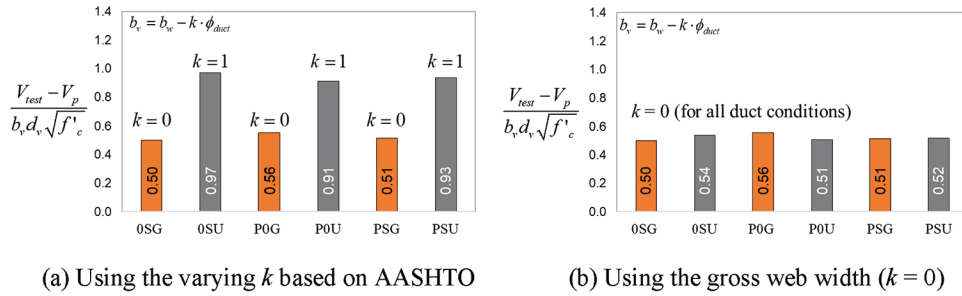


(a) Initial cracking at  $V_{LC}$



(b) Vertical strain development

Fig. 10—Analysis of service-level loading.



(a) Using the varying  $k$  based on AASHTO

(b) Using the gross web width ( $k = 0$ )

Fig. 11—Normalized ultimate shear stress.

Table 4—Service-level cracking for grouted and ungrouted specimens

Specimen ID		$V_{LC}$ , kip (kN)	$V_{tests}$ , kip (kN)	$V_{LC}/V_{test}$	Normalized shear stress*
Grouted specimens	Tx62-0SG	403 (1793)	855 (3803)	0.47	0.18
	Tx62-P0G	418 (1859)	1082 (4813)	0.39	0.19
	Tx62-PSG	383 (1704)	1011 (4497)	0.38	0.16
Ungrouted specimens	Tx62-0SU	352 (1566)	961 (4275)	0.37	0.15
	Tx62-P0U	411 (1828)	966 (4297)	0.43	0.18
	Tx62-PSU	381 (1695)	1005 (4470)	0.38	0.17

\*Normalized shear stress calculated as  $(V_{LC} - V_p)/(b_w d_v \sqrt{f'_c})$ , unitless.

serviceability analysis, this study monitored the occurrence of cracking within the test span using the strain development of the surface gauge. Figure 10(b) shows the vertical strain development containing the change point of distinctly elevated strain. This change point of shear load level ( $V_{LC}$ ) was validated by the visual inspection for the occurrence of initial hairline cracks.

Table 4 presents the analysis of serviceability in terms of the shear force for the service-level crack ( $V_{LC}$ ) based on the change point by using the surface gauge, the ratio of  $V_{LC}$  to  $V_{tests}$ , and normalized shear stress. The ratio of  $V_{LC}$  to  $V_{tests}$  roughly mirrors the reference level of 0.5, as suggested by the Bircher model. Nevertheless, it presents challenges when comparing the serviceability of test specimens between grouted and ungrouted ducts due to the variations in the concrete strengths. To address this issue, the normalization of shear stress at the level of service load was implemented using Eq. (12).

$$v_{LC} = \frac{V_{LC} - V_p}{b_w d_v \sqrt{f'_c}} \quad (12)$$

The normalized shear stress ( $v_{LC}$ ) of both grouted and ungrouted specimens indicated similar stress levels ranging from 0.15 to 0.19 to trigger the onset of the diagonal shear cracks in the post-tensioning duct area. In other words, no difference in serviceability performance was observed regardless of the duct condition. These results align with the theoretical service-load levels by the Bircher model.

### Ultimate level

The failure loads obtained from each pair of tests were within 5% of each other. For clarity, the average failure load from each pair of tests is used for the comparison with AASHTO LRFD shear resistance. Figure 7 reports the ultimate shear loads for each specimen; however, the comparison analysis of the ultimate shear capacity for each specimen could be obscured without normalization. As such, the ultimate shear stress was normalized by using Eq. (13).

$$v_{normal} = \frac{V_{test} - V_p}{b_w d_v \sqrt{f'_c}} \quad (13)$$

The coefficient of effective web width ( $k$ ) plays a pivotal role in estimating the shear capacity of the post-tensioned concrete member. For example, the current edition of AASHTO LRFD<sup>5</sup> establishes different values for  $k$  based on the filler condition of the duct due to the different internal stress flows, as shown in Fig. 9. Accordingly, Fig. 11(a) shows the normalized shear stress calculated using the effective web width ( $b_v$ ), which applies the appropriate values of  $k$  to the specimens containing grouted and ungrouted ducts, respectively. It clearly indicates that, using the current AASHTO LRFD procedure, higher shear stress levels are calculated for the specimens with ungrouted ducts than for the grouted ones. Further, Fig. 11(b) shows the normalized shear stress calculated using the gross web width ( $k = 0$ ) regardless of the duct condition. Remarkably, all test specimens are calculated to develop a similar level of normalized shear stress.

The survey of the cracking in the web revealed well-distributed, fan-shaped shear cracks for all test specimens. This indicates that the entire web engages in the shear force-resistance mechanism (for example,  $k = 0$ ). As the cracked concrete component carries shear through the aggregate interlock at the crack interfaces, similar patterns of diagonal cracking could expect a similar shear resistance from the effect of aggregate interlock on the cracks.<sup>30</sup> Consequently, similar web-width correction factors should be considered for both grouted and ungrouted ducts. To further understand the shear mechanism of post-tensioned concrete members and to determine appropriate values for  $k$ , the web behavior is further analyzed in the following section.

### Experimental versus AASHTO LRFD shear resistance

The experimental shear resistance,  $V_{test}$ , was calculated at the critical section based on the measured ultimate load from each test. Specimen properties, such as prestress loss,

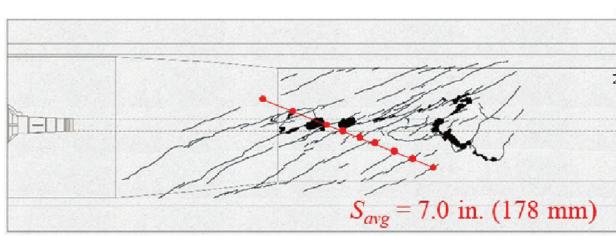
material, and geometry conditions, were used to calculate the nominal shear resistance,  $V_n$ , using the current AASHTO LRFD.<sup>5</sup> Table 5 presents the comparison between the experimental shear resistance,  $V_{test}$ , and the calculated resistance using the AASHTO LRFD shear design,  $V_n$ . Moreover, information on reduction factors, such as the web-width reduction factor,  $k$ , duct diameter correction factor,  $\delta$ , and shear-strength reduction factor,  $\lambda_{duct}$ , are provided to evaluate the current version of shear strength design according to the AASHTO LRFD provisions. Because the primary purpose of this procedure is to evaluate the nominal shear capacity of test girders, the load and resistance factors were taken as 1.0. The experimental capacities of the specimens with grouted ducts were, on average, 30% larger than the calculated capacities. This level of conservatism is generally regarded as adequate for shear-critical specimens based on the shear test database research.<sup>31</sup> On the contrary, the calculated capacities for the specimens with ungrouted ducts produced capacity estimates with a smaller safety margin, averaging approximately 10%. Therefore, the shear-strength reduction factors associated with ungrouted ducts need to be revised to ensure consistent levels of conservatism compared to the grouted case. This revision is crucial to maintain a balanced and reliable design approach for post-tensioned concrete members.

### DEVELOPMENT OF DESIGN RECOMMENDATIONS

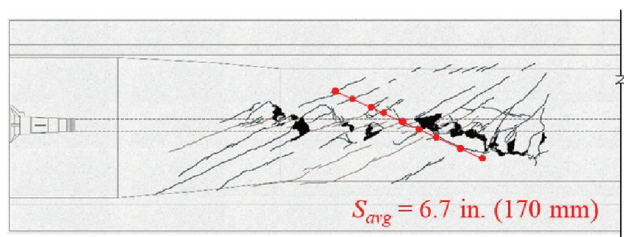
This section presents the development of shear design recommendations for the post-tensioned girders that incorporate the effects of grouted and ungrouted ducts on the shear-resistance mechanism. The proposed changes to the shear design of post-tensioned members are founded on the experimental observations made in this study and are further supplemented by relevant data available from tests conducted by Moore et al.<sup>10</sup> For detailed information about

**Table 5—Test results summary with ratio of test results to nominal shear resistance**

Specimen ID	$k$	$\delta$	$\lambda_{duct}$	$V_n$	$V_{test}$	$V_{test}/V_n$
	Web-width reduction	Duct diameter correction	Shear-strength reduction	Nominal shear resistance, kip (kN)	Shear strength, kip (kN)	Ratio
Tx62-OSG	0	2	0.605	694 (3087)	879 (3910)	1.27
Tx62-P0G	0	2	0.605	766 (3407)	1066 (4742)	1.39
Tx62-PSG	0	2	0.605	809 (3599)	1009 (4488)	1.25
Tx62-0SU	1	0	1.000	816 (3629)	948 (4217)	1.16
Tx62-P0U	1	0	1.000	891 (3963)	966 (4297)	1.08
Tx62-PSU	1	0	1.000	919 (4087)	990 (4404)	1.08



(a) Tx62-OSG



(b) Tx62-0SU

Fig. 12—Crack propagation and average crack spacing at ultimate load level.

the test specimen configurations and specifics, please refer to Appendix C.

**Proposed modification for calculation of  $V_{n1} = V_c + V_s + V_p$**

*Effective web-width factor,  $b_v$* —Figure 12 depicts the surveyed crack patterns for the specimens with straight grouted and ungrouted ducts. Well-distributed, fan-shaped diagonal cracks developed, which had similar average crack spacings regardless of the duct condition. Similar cracking patterns were observed for all test specimens. Also, the average crack spacing observed ranged from 6.5 to 7.0 in. (16.5 to 17.8 cm)—findings that align closely with the estimations provided by Collins and Mitchell,<sup>2</sup> which predict an average crack spacing of 6.4 in. (16.3 cm) for all specimens, as calculated using Eq. (14).

$$s_m = 2\left(c + \frac{s_2}{10}\right) + k_1 k_2 \frac{d_b}{\rho_{ef}} \quad (14)$$

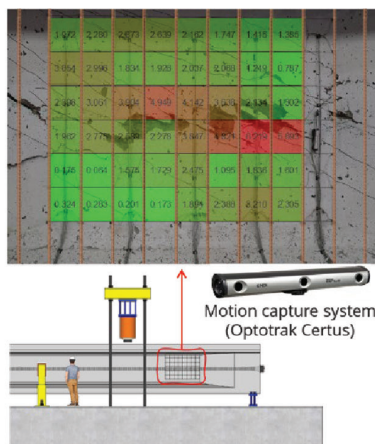
This indicated that the entire web engaged in the shear force-resisting mechanism and provided insight into the calculation of the concrete contribution to the nominal shear resistance.

Moreover, the strains were monitored during the structural test using the aforementioned motion-capture system, shown in Fig. 13(a). The average strains from the selected quadrilateral web region, sized 24 x 24 in. (610 x 610 mm),

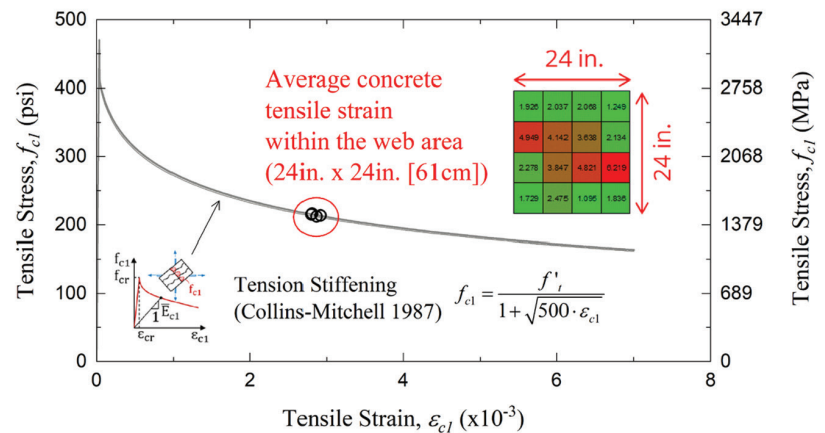
were used to calculate the residual tensile stresses in the cracked concrete component using the Collins-Mitchell 1987 model.<sup>32</sup> Figure 13(b) shows the post-cracking tensile stresses calculated for specimens of Tx62-0SG, 0SU, P0G, and PSU, indicating similar performance. This leads to the conclusion that the disparities are negligible in terms of the value of the average tensile strains and the concrete tensile stresses between specimens with grouted and ungrouted ducts. Therefore, the effective web-width correction factor,  $k$ , in AASHTO LRFD<sup>5</sup> should be updated to the value of zero for both grouted and ungrouted conditions, to reflect the engagement of the gross web width ( $b_w$ ), based on the results and numerical analysis.

In summary, the following conclusions can be made based on the development of cracks and the state of post-cracking concrete tensile stress:

- The entire web engages the shear-transfer mechanism, as indicated by the occurrence of well-distributed, fan-shaped diagonal shear cracks for specimens with either grouted or ungrouted ducts.
- No significant difference was observed between the specimens with grouted and ungrouted ducts with respect to the post-cracking tensile stresses of the concrete component.
- As such, the gross web width,  $b_w$ , should be used in the calculation of the concrete contribution to the shear strength capacity.

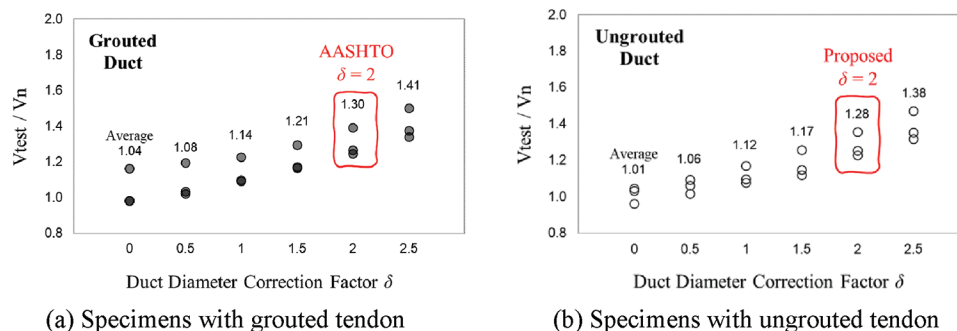


(a) Vision system monitoring test span



(b) State of tensile stress

Fig. 13—State of residual tensile stress using motion-capture system. (Note: 1 in. = 25.4 mm.)



(a) Specimens with grouted tendon

(b) Specimens with ungrouted tendon

Fig. 14—Determination of duct diameter correction factor,  $\delta$ .



*Duct diameter correction factor,  $\delta$* —Figure 14 shows the variation of the experimental-to-calculated ratios as a function of the duct diameter correction factor,  $\delta$ , in the grouted and ungrouted tendons, respectively. For  $\delta$  taken as 2.0, the same level of conservatism is achieved for specimens with ungrouted ducts as for those with grouted ducts. Based on the changes proposed for the effective web-width correction factor ( $k$ ), the proposed value of 2.0 for the duct diameter correction factor ( $\delta$ ) ensures similar structural conservativeness in both grouted and ungrouted tendons. Note that this study's proper conservative level (approximately 30%) is in agreement with the data-driven shear test database research.<sup>31</sup>

**Proposed modification for calculation of  $V_{n2} = 0.25f'_c b_v d_v$**

The nominal shear resistance ( $V_{n2}$ ) limits the shear stress level to  $0.25f'_c$  to avoid compressive failure of the concrete, as suggested by Bentz et al.<sup>13</sup> All test specimens experienced localized web-crushing failure in the vicinity of the post-tensioning duct at the ultimate load level, regardless of whether ducts were grouted or ungrouted, as illustrated in Fig. 15. The current edition of AASHTO LRFD uses different values for  $k$  for bonded tendons as the gross web width ( $k = 0$ ) and unbonded tendons as the effective web width ( $k = 1$ ). This approach is not in agreement with the test results, which indicate similar failure mechanisms.

Specifically, the value of  $k$  is 0.0 for bonded tendons, as stiff grout is assumed to resist the intruding compressive stress. On the other hand,  $k$  is 1.0 for unbonded tendons because the

empty duct is expected to redirect the internal stress flow, potentially decreasing the resistance of compressive force, as shown in Fig. 16(a). Nevertheless, this assumed internal stress flow is only validated in the condition of elasticity and linear behavior, which implies no growth of macrocracks in the concrete component.

This study surveyed the cracking at the critical section by cutting the tested specimen, as conceptually illustrated in Fig. 16(b). Three cracking patterns were identified: 1) the horizontal crack, which is the inclined shear crack; 2) localized web crushing; and 3) internal cracks around the duct due to the splitting force. When the internal cracks form around the duct, they decrease the bond strength between the duct and adjacent concrete. At the ultimate load level, accounting for the plasticity in the post-tensioned girder, this debonded condition redirects the internal compressive stress flow toward the outside of the cross section, similar to unbonded tendons. This plasticity mechanism approach is rational because the nominal shear resistance should be determined at the moment of ultimate load level.

The motion-capture system data at the ultimate load level were used to calculate the principal strains ( $\epsilon_1$  and  $\epsilon_2$ ) in two quadratic regions: the web (24 x 24 in. [610 x 610 mm]) and the duct (6 x 6 in. [152 x 152 mm]) at the critical section. The Vecchio-Collins compression-softening model<sup>33</sup> was used to calculate the compressive stress of web and duct regions, respectively, as shown in Fig. 17(a). This state of compressive stress and strain indicates that the duct region typically crushes locally before the rest of the web region, which is located in the plateau of compression softening. Moreover,

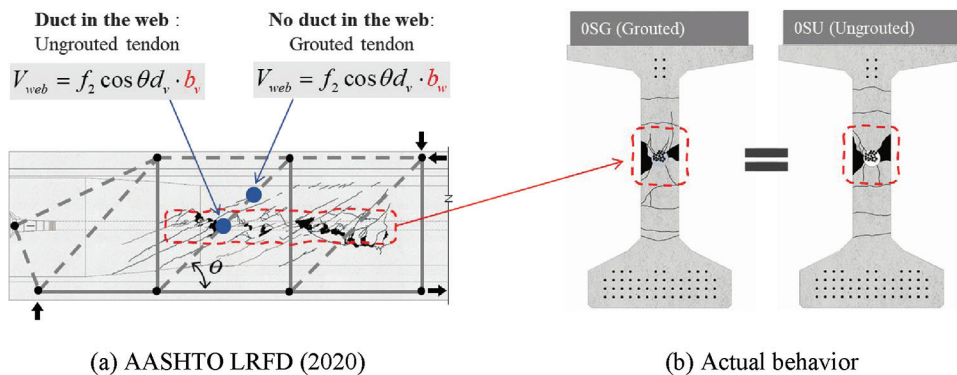


Fig. 15—Ultimate failure mode of localized web crushing in specimens with grouted or ungrouted ducts.

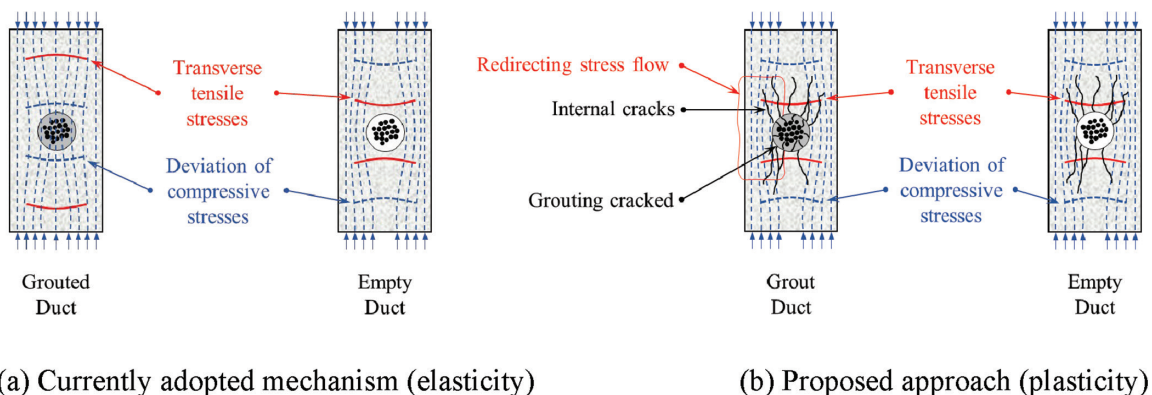


Fig. 16—Conceptual theory of internal stress flow for bonded and unbonded tendons.

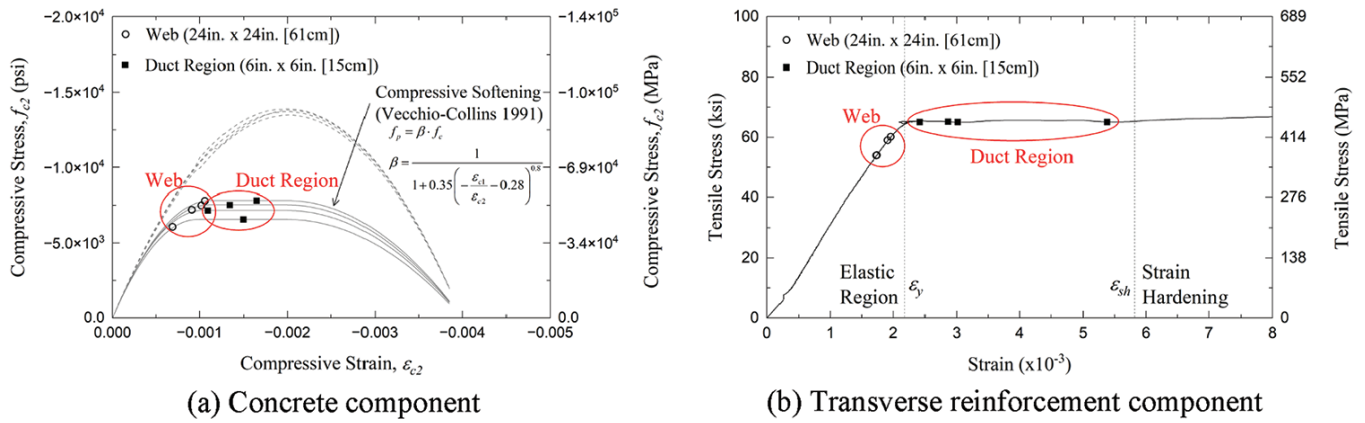


Fig. 17—State of stress condition in each component. (Note: 1 in. = 25.4 mm.)

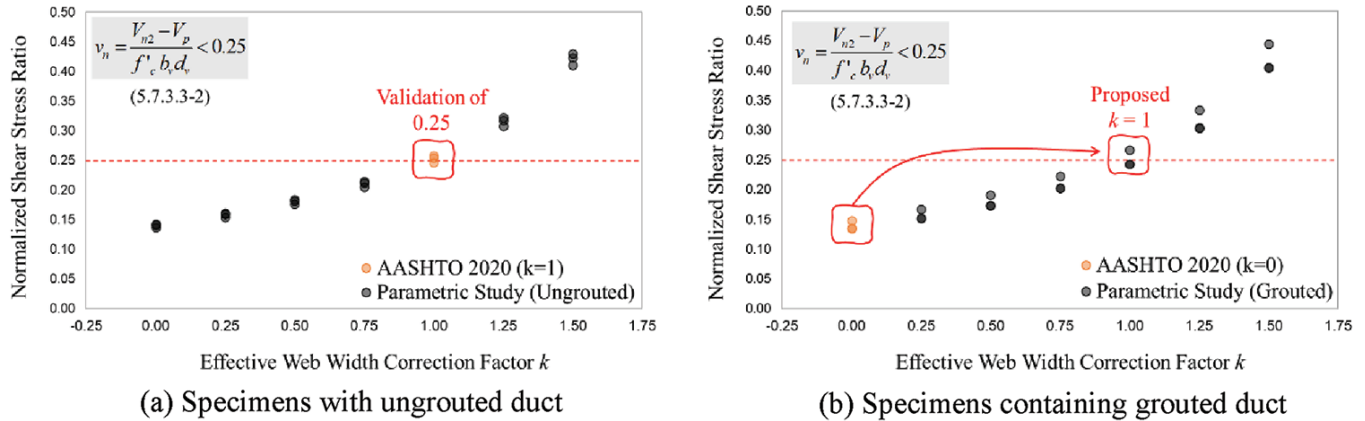


Fig. 18—Normalized shear stress level using structural test with respect to effective web-width correction factor,  $k$ .

this analysis predicted similar failure modes regardless of the tendon conditions, which aligns with the test results.

In the same manner, the strength contribution of the transverse reinforcement can be determined, as shown in Fig. 17(b). Using the average vertical strain ( $\epsilon_y$ ), the transverse reinforcement at the duct region is highly expected to yield (that is, yield strain of 0.0022) based on the stress and strain curve from the material test of the reinforcing bar. The stress levels of the concrete and transverse reinforcement components show the failure mode was initiated by yielding of the transverse reinforcement and localized web crushing. This numerical analysis reflects the failure modes from the test results, as shown in Fig. 15. It is important to note that Bentz et al.<sup>13</sup> assumed small concrete compression strains (that is, within the linear-elastic region) in their original derivation that led to Eq. (2). However, Fig. 17 shows that the estimated strains in the girder webs are in the nonlinear region. The condition of the duct for  $V_{n2}$  will be discussed in the following section, as this research proposes the effective web-width correction factor ( $k$ ).

To determine the proper value of the effective web-width correction factor,  $k$ , the normalized shear stress using Eq. (15) was computed with respect to  $k$ . Because  $V_{n2}$  was related to the concrete compressive strength, the normalization should apply the compressive strength of concrete,  $f'_c$  in Eq. (15).

$$v_{normal} = \frac{V_{n2} - V_p}{f'_c b_v d_v} \quad (15)$$

Figure 18 shows the results of a parametric study performed. The shear stress level for specimens with ungrouted ducts has a value equal to  $0.25f'_c$  when  $k = 1.0$ , corresponding to the current AASHTO LRFD value for  $k$ . Based on the internal stress profile shown in Fig. 16, a value of 1.0 for  $k$  is reasonable for an ungrouted duct, reflecting the localized web crushing in the test specimen.

On the other hand, the shear stress levels calculated for the specimens with grouted tendons using the current edition of AASHTO LRFD ( $k = 0$ ) are below the value of  $0.25f'_c$  (approximately 0.15 normalized shear stress ratio). These results disagree with the failure mode observed during the test: web crushing at the onset of transverse reinforcement yielding. To address this issue, this study proposes using a value of 1.0 for  $k$ , leading to calculated normalized shear stress levels in the range of  $0.25f'_c$ , as per Fig. 18(b). This recommendation also aligns with the internal stress flow, as shown in Fig. 16, considering plasticity in the concrete girder containing the post-tensioning duct.

The following conclusions can be drawn:

- The level of concrete compressive stress determined using the Vecchio-Collins compression-softening model<sup>33</sup> justifies the experimentally observed web crushing for specimens with either grouted or ungrouted ducts.

**Table 6—Proposed modification for shear design of girders with post-tensioned ducts**

	AASHTO LRFD <sup>5</sup>		Proposed modification	
Nominal shear resistance $V_n^*$	$V_{n1} = V_c + V_s + V_p$	$V_{n2} = 0.25f_c'b_vd_v$	$V_{n1} = V_c + V_s + V_p$	$V_{n2} = 0.25f_c'b_vd_v$
Effective web-width correction factor, $b_v = b_w - k \cdot \phi_{duct}$	$k = 0$ (grouted) $k = 1$ (ungrouted)	$k = 0$ (grouted) $k = 1$ (ungrouted)	$k = 0$ (grouted) <b><math>k = 0</math></b> <sup>†</sup> (ungrouted)	<b><math>k = 1</math></b> <sup>†</sup> (grouted) $k = 1$ (ungrouted)
Duct diameter correction factor, $\lambda_{duct} = 1 - \delta \cdot \left(\frac{\phi_{duct}}{b_w}\right)^2$	$\delta = 2$ (grouted) $\delta = 0$ (ungrouted)	Not applicable	$\delta = 2$ (grouted) <b><math>\delta = 2</math></b> <sup>†</sup> (ungrouted)	Not applicable

\* $V_n$  is determined by lesser of  $V_{n1}$  and  $V_{n2}$ .

<sup>†</sup>Proposed coefficient based on results of this study in bold with underline.

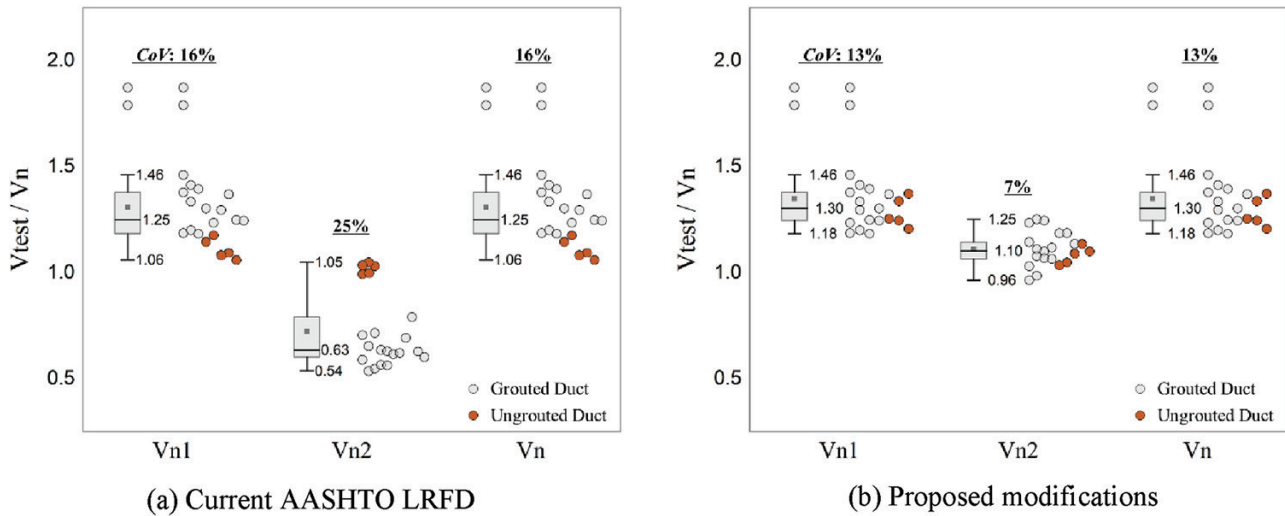


Fig. 19—Calculation of nominal shear resistance.

- The tested specimens containing ungrouted ducts experienced the localized web crushing at the normalized shear stress level of  $0.25f_c'$ .
- When  $k$  equals 1.0, as proposed, the shear stress level at the failure of specimens with grouted ducts becomes similar to that of specimens with ungrouted ducts. This aligns well with the failure mode of localized web crushing.

### Evaluation of proposed modifications

Table 6 presents a summary of the proposed modifications to the current edition of AASHTO LRFD.<sup>5</sup> The proposed modifications have a similar approach to the shear design of post-tensioned systems with grouted and ungrouted ducts. They include: 1) the shear-strength reduction factor,  $\lambda_{duct}$ , should be used in the calculation of the transverse reinforcement contribution,  $V_s$ , to the nominal shear resistance; 2) the gross web width,  $b_w$ , should be used in the calculation of the concrete contribution,  $V_c$ , to the nominal shear resistance,  $V_{n1}$ ; and 3) the upper limit on the nominal shear resistance ( $V_{n2} = 0.25f_c'b_vd_v$ ) should be calculated using the effective web width,  $b_v$ , reduced to account for the presence of the duct.

Figure 19 shows the comparison between the shear-strength predictions obtained using the current AASHTO LRFD shear design equations and the proposed modifications, in terms of experimental-to-calculated ratios. The proposed changes were derived from the findings and

in-depth analyses of the results of the experimental program undertaken from this study, as well as additional relevant test data reported in the literature.<sup>10</sup>

The results of both  $V_{n1} = V_c + V_s + V_p$  and  $V_{n2} = 0.25f_c'b_vd_v$  are shown, and the lesser value,  $V_n$ , is given in the third column. The coefficient of variance ( $CoV$ ) decreases for the predictions obtained employing the proposed modifications while maintaining a level of structural conservativeness similar to the current AASHTO LRFD equations. In addition, the results obtained for  $V_{n2} = 0.25f_c'b_vd_v$  employing the proposed modifications are in significantly better agreement with the experimental results, with a ratio of  $V_{test}/V_n = 1.10$ , compared to the current AASHTO LRFD equation, which stands at  $V_{test}/V_n = 0.63$ . For all specimens, the calculated values for  $V_{n1}$  were lower than the values obtained for  $V_{n2}$ ; as such, the nominal shear resistances,  $V_n$ , have the values of  $V_{n1}$ . In essence, the introduced modifications manifest a significant enhancement in the reliability of shear design equations applicable to post-tensioned concrete elements, as evidenced by the reduction in  $CoV$  from 16% to 13% for  $V_{n1}$  and from 25% to 7% for  $V_{n2}$ .

### SUMMARY AND CONCLUSIONS

A comprehensive experimental program was undertaken to investigate the shear behavior of post-tensioned concrete members with post-tensioning ducts, selecting the grouting conditions and duct layout as test variables. The experimental program involved the construction and testing of



six Tx62 I-girder specimens. The structural tests resulted in similar failure modes, initiated by localized web crushing, regardless of the duct condition and tendon profile. The extensive instrumentation that monitored the experimental behavior of the specimens provided valuable insight into the underlying mechanisms that governed the response. These tests serve as a foundation for the proposed changes to the shear resistance calculation in AASHTO LRFD.

### Summary of experimental results and discussion

- This study found that all test specimens experienced a similar failure mechanism regardless of the tendon condition (bonded or unbonded) and profile (straight, parabolic, or hybrid).
- Around the duct area, the vibrating-wire gauges (VWGs) measured increasing tensile strains in the out-of-plane direction for both grouted and ungrouted duct conditions.
- In the analysis of service-level cracking, the normalized shear stress of both grouted and ungrouted conditions indicated similar stress levels to trigger the onset of the diagonal shear cracks in the post-tensioning duct area.
- All test specimens developed similar levels of normalized shear stress at the ultimate load level.

### Summary of development of design recommendations

- The entire web engaged the shear-transfer mechanism based on the occurrence of well-distributed, fan-shaped diagonal shear cracks for specimens with either grouted or ungrouted tendons.
- No significant difference was found between the grouted and ungrouted tendons with respect to the aggregate interlock force based on the numerical analysis using the Collins-Mitchell 1987 model.<sup>32</sup>
- As such, the gross web width,  $b_w$ , should be used in the calculation of the concrete component,  $V_c$ , to the shear strength capacity.
- The level of concrete compressive stress determined using the Vecchio-Collins compression-softening model<sup>33</sup> justifies the experimentally observed web crushing for specimens with either grouted or ungrouted tendons.
- The specimens containing ungrouted tendons experienced localized web crushing at the normalized shear stress level of  $0.25f'_c$ .
- When  $k$  equals 1.0, as proposed, the calculated shear stress level at failure of specimens with grouted tendons is similar to that of specimens with ungrouted tendons. This aligns well with the failure mode of localized web crushing.

### Proposed changes to AASHTO LRFD

The current AASHTO LRFD provisions for the shear design of post-tensioned concrete members account for a reduction in the shear capacity due to the detrimental effect caused by the presence of ducts in the web region, varying based on the condition of the ducts. The current shear design procedure was not found to align with the observed failure

mechanism of the post-tensioned concrete members. This led to the following proposed modifications:

- The entire web engages the shear-transfer mechanism, regardless of whether the specimen's tendons are grouted or ungrouted. As such, the gross web width ( $b_w$ ) should be used in the calculation of the concrete component to the shear strength capacity for  $V_{n1}$ , Eq. (5.7.3.3-1) in AASHTO LRFD.<sup>5</sup>
- The normalized shear stress level of specimens containing grouted tendons is similar to that of specimens with ungrouted tendons when the value of  $k$  is 1.0, as proposed. This is in agreement with the observed failure mode, localized web crushing. Thus, when calculating  $V_{n2}$ , Eq. (5.7.3.3-2) in AASHTO LRFD, the effective web width ( $b_v$ ) should be reduced by the diameter of the duct.<sup>5</sup>
- Based on the changes proposed for the effective web-width correction factor ( $k$ ), the proposed value of 2.0 for the duct diameter correction factor ( $\delta$ ) ensures similar structural conservativeness for both grouted and ungrouted tendons.

### AUTHOR BIOS

**Sangyoung Han** is an Assistant Professor in the Department of ICT Integrated Ocean Smart City Engineering at Dong-A University, Busan, South Korea. He received his PhD from The University of Texas at Austin, Austin, TX. His research interests include the concrete mixture characteristics and analysis of reinforced and prestressed concrete structures.

**Jarrod Zaborac** is a Graduate Engineer in the Diagnostics Group at Walter P Moore in Austin, TX. He received his PhD from The University of Texas at Austin in 2021.

ACI member **Jongkwon Choi** is an Assistant Professor in the Department of Civil and Environmental Engineering at Hongik University, Seoul, South Korea. He received his BS and MS from Seoul National University, Seoul, South Korea, and his PhD from The University of Texas at Austin. His research interests include the mechanical behavior, experiments, and analysis of reinforced concrete and prestressed concrete structures, and structural assessment of aging concrete structures.

**Anca C. Ferche** is an Assistant Professor in the Department of Civil, Architectural and Environmental Engineering at The University of Texas at Austin. She received her PhD from the University of Toronto, Toronto, ON, Canada. She is a member of Joint ACI-ASCE Committee 447, Finite Element Analysis of Reinforced Concrete Structures. Her research interests include performance assessment and analysis of reinforced concrete structures, concrete deterioration mechanisms, and sustainability of concrete structures.

**Oguzhan Bayrak**, FACI, is a University Distinguished Professor in the Department of Civil, Architectural and Environmental Engineering, where he serves as the Director of the Concrete Bridge Engineering Institute and holds the Cockrell Family Chair in Engineering No. 20, at The University of Texas at Austin. He is a member of ACI Committees S803, Faculty Network Coordinating Committee, and 341, Performance-Based Seismic Design of Concrete Bridges, and Joint ACI-ASCE Committees 441, Reinforced Concrete Columns, and 445, Shear and Torsion.

### ACKNOWLEDGMENTS

The authors are grateful to the Texas Department of Transportation (TxDOT) for providing funds to conduct this research study (Report No. FHWA/TX-22/5-6652-01-1, Grant No. 5-6652-01). The contributions of the Project Monitoring Committee—J. Steele (Project Manager), C. Gutierrez, G. Turco, J. Tucker, J. Roche, L. Flournoy, and M. Hyzak—are deeply appreciated. Many thanks are due to Valley Prestress Products, Inc., in Eagle Lake, TX, for fabricating the girders that were used for the experimental program. Special thanks are also offered to the numerous students and staff members at Ferguson Structural Engineering Laboratory for ensuring the successful completion of the research study.

## NOTATION

$A_{cef}$	=	area of effective embedment zone of concrete where reinforcing bars can influence crack width
$A_s$	=	area of steel considered to be effectively bonded to concrete
$A_v$	=	area of transverse reinforcement within distance $s$
$b_v$	=	effective web width
$b_w$	=	gross web width
$c$	=	clear concrete cover
$d_b$	=	bar diameter
$d_v$	=	effective shear depth
$f'_c$	=	compressive strength of concrete for use in design, and $\beta$ indicates ability of diagonally cracked concrete to transmit tension and shear
$f_y$	=	specified minimum yield strength of reinforcement
$f_2$	=	average principal (diagonal) compressive stress
$k$	=	effective web-width correction factor
$k_1$	=	coefficient that characterizes bond properties of bars ( $k_1 = 0.4$ for deformed bars and $k_1 = 0.8$ for plain bars)
$k_2$	=	coefficient to account for strain gradient, $k_2 = 0.25(\epsilon_1 + \epsilon_2)/2\epsilon_1$ ( $\epsilon_1$ and $\epsilon_2$ are largest and smallest tensile strains in effective embedment zone, respectively)
$s$	=	spacing of transverse reinforcement
$s_2$	=	maximum spacing between longitudinal reinforcing bar but shall not be taken greater than $15d_b$
$V_n$	=	nominal shear resistance
$V_{n1}$	=	nominal shear resistance given in Eq. (5.7.3.3-1)
$V_{n2}$	=	nominal shear resistance given in Eq. (5.7.3.3-2)
$V_p$	=	vertical component of prestressing force
$V_{test}$	=	maximum shear force carried by test specimen
$\alpha$	=	angle of inclination of transverse reinforcement to longitudinal axis
$\beta$	=	factor indicating ability of diagonally cracked concrete to transmit tension and shear
$\delta$	=	duct diameter correction factor
$\epsilon_x$	=	average longitudinal strain acting on member
$\epsilon_y$	=	average vertical strain acting on member
$\epsilon_1$	=	average principal tensile strain of concrete acting perpendicular to principal diagonal tensile stress
$\epsilon_2$	=	average principal compressive strain of concrete in direction of principal diagonal compressive stress
$\phi$	=	shear-resistance factor
$\phi_{duct}$	=	duct diameter
$\lambda_{duct}$	=	accounts for reduction in shear strength due to presence of post-tensioning duct in thin web
$\theta$	=	angle of inclination of diagonal compressive stresses
$\rho_{ef}$	=	$A_s/A_{cdf}$

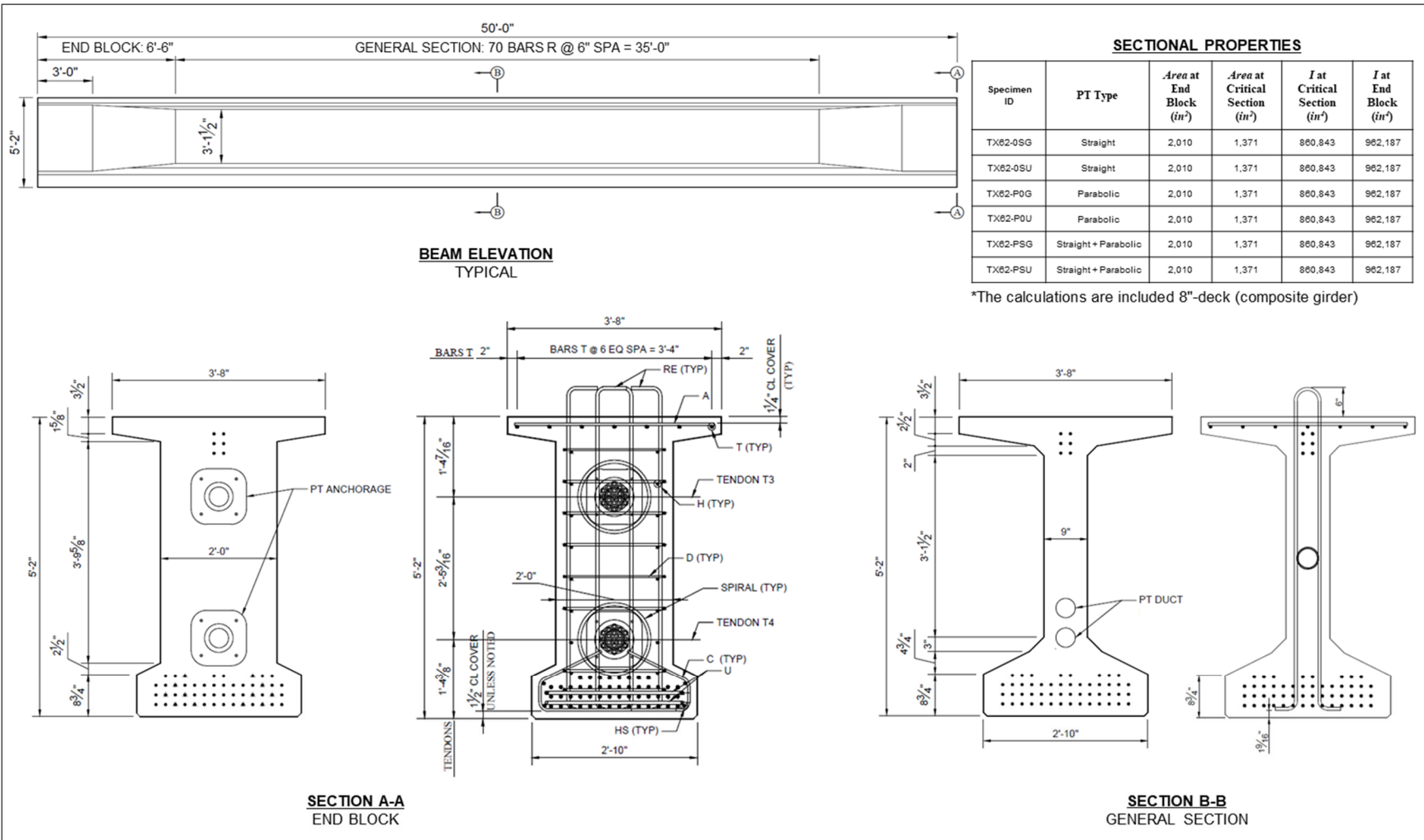
## REFERENCES

- Castrodale, R. W., and White, C. D., "Extending Span Ranges of Precast Prestressed Concrete Girders," NCHRP Report 517, Transportation Research Board, Washington, DC, 2004, 603 pp.
- Collins, M. P., and Mitchell, D., *Prestressed Concrete Structures*, Prentice Hall, Englewood Cliffs, NJ, 1991, 766 pp.
- FDOT, "New Directions for Florida Post-Tensioned Bridges," Florida Department of Transportation, Tallahassee, FL, 2004, 95 pp.
- Hamilton, H. R.; Rice, J. A.; Abdullah, A. B. M.; Bhatia, R.; Brenkus, N.; and Skelton, D., "Replaceable Unbonded Tendons for Post-Tensioned Bridges," Florida Department of Transportation, Tallahassee, FL, 2017, 669 pp.
- AASHTO, "AASHTO LRFD Bridge Design Specifications," ninth edition, American Association of State Highway and Transportation Officials, Washington, DC, 2020, 1914 pp.
- AASHTO, "Guide Specifications for Design and Construction of Segmental Concrete Bridges," second edition, American Association of State Highway and Transportation Officials, Washington, DC, 1999, 96 pp.
- PCI, "PCI Bridge Design Manual (MNL-133-14)," third edition, Precast/Prestressed Concrete Institute, Chicago, IL, 2014, 1620 pp.
- EN 1992-1-1:2004, "Eurocode 2: Design of Concrete Structures - Part 1-1: General Rules and Rules for Buildings," European Committee for Standardization, Brussels, Belgium, 2004, 225 pp.
- fib, "fib Model Code for Concrete Structures 2010," International Federation for Structural Concrete, Lausanne, Switzerland, 2013, 434 pp.
- Moore, A.; Williams, C.; Al-Tarafany, D.; Felan, J.; Massey, J.; Nguyen, T.; Schmidt, K.; Wald, D.; Bayrak, O.; Jirsa, J.; and Ghannoum, W., "Shear Behavior of Spliced Post-Tensioned Girders," Report No. FHWA/

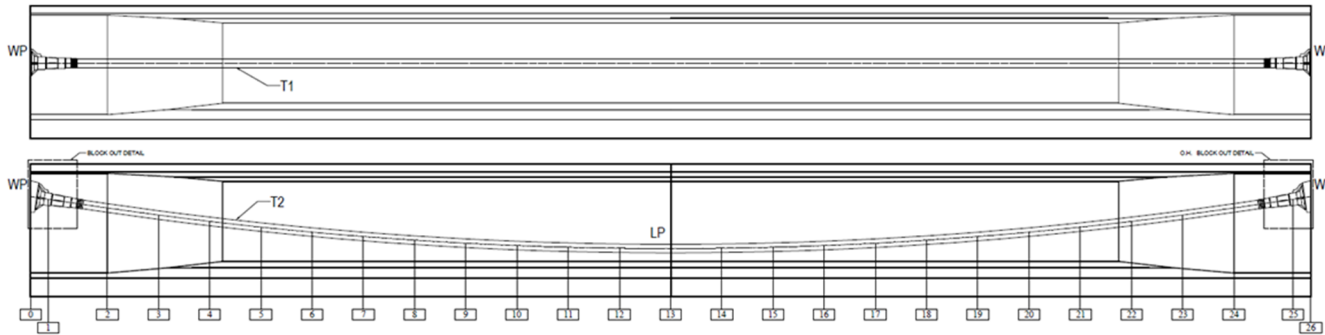
TX-14/0-6652-1, Center for Transportation Research, The University of Texas at Austin, Austin, TX, 2015, 220 pp.

- Skelton, D., and Hamilton, H. R., "Shear Behavior of Webs Post-Tensioned with Tendons Containing Flexible Fillers," Florida Department of Transportation, Tallahassee, FL, 2021, 198 pp.
- Vecchio, F. J., and Collins, M. P., "The Modified Compression-Field Theory for Reinforced Concrete Elements Subjected to Shear," *ACI Journal Proceedings*, V. 83, No. 2, Mar.-Apr. 1986, pp. 219-231.
- Bentz, E. C.; Vecchio, F. J.; and Collins, M. P., "Simplified Modified Compression Field Theory for Calculating Shear Strength of Reinforced Concrete Elements," *ACI Structural Journal*, V. 103, No. 4, July-Aug. 2006, pp. 614-624.
- Muttoni, A.; Burdet, O. L.; and Hars, E., "Effect of Duct Type on the Shear Strength of Thin Webs," *ACI Structural Journal*, V. 103, No. 5, Sept.-Oct. 2006, pp. 729-735.
- Wald, D. M.; Moore, A.; Bayrak, O.; and Jirsa, J. O., "Compressive Behavior of Concrete Panels Containing Steel and Plastic Ducts," *ACI Structural Journal*, V. 114, No. 5, Sept.-Oct. 2017, pp. 1167-1176. doi: 10.14359/51689721
- Kuchma, D., "Effect of Ducts on Shear Strength of Prestressed and Non-Prestressed Members [Interview] (15 June 2013)," The University of Texas at Austin, Austin, TX, 2013.
- WSDOT, "Bridge Design Manual LRFD," Washington State Department of Transportation, Olympia, WA, 2023, 1050 pp.
- TxDOT, "Bridge Design Manual - LRFD," Texas Department of Transportation, Austin, TX, 2021, 95 pp.
- Garber, D.; Gallardo, J.; Deschenes, D.; Dunkman, D.; and Bayrak, O., "Effect of New Prestress Loss Estimates on Pretensioned Concrete Bridge Girder Design," Report No. FHWA/TX-12/0-6374-2, Center for Transportation Research, The University of Texas at Austin, Austin, TX, 2013, 300 pp.
- Han, S.; Zaborac, J.; Webb, Z. D.; Choi, J.; Ferche, A. C.; and Bayrak, O., "Shear Behavior of Spliced Post-Tensioned Girders with UngROUTED Tendons," Report No. FHWA/TX-22/5-6652-01-1, Center for Transportation Research, The University of Texas at Austin, Austin, TX, 2022, 181 pp.
- ASTM C39/C39M-14, "Standard Test Method for Compressive Strength of Cylindrical Concrete Specimens," ASTM International, West Conshohocken, PA, 2014, 7 pp.
- ASTM A615/A615M-20, "Standard Specification for Deformed and Plain Carbon-Steel Bars for Concrete Reinforcement," ASTM International, West Conshohocken, PA, 2020, 8 pp.
- ASTM A416/A416M-18, "Standard Specification for Low-Relaxation, Seven-Wire Steel Strand for Prestressed Concrete," ASTM International, West Conshohocken, PA, 2018, 5 pp.
- AISC, "Steel Construction Manual," 15th edition, American Institute of Steel Construction, Chicago, IL, 2017, 2324 pp.
- Moore, A. M.; Williams, C. S.; Massey, J. B.; Bayrak, O.; Ghannoum, W. M.; and Jirsa, J. O., "Shear Behavior of Post-Tensioned Girders," *ACI Structural Journal*, V. 114, No. 6, Nov.-Dec. 2017, pp. 1615-1625. doi: 10.14359/51700835
- ASTM C496-96, "Standard Test Method for Splitting Tensile Strength of Cylindrical Concrete Specimens," ASTM International, West Conshohocken, PA, 1996, 4 pp.
- ACI Committee 318, "Building Code Requirements for Structural Concrete (ACI 318-19) and Commentary (ACI 318R-19) (Reapproved 2022)," American Concrete Institute, Farmington Hills, MI, 2019, 624 pp.
- ACI Committee 224, "Control of Cracking in Concrete Structures (ACI 224R-01) (Reapproved 2008)," American Concrete Institute, Farmington Hills, MI, 2001, 46 pp.
- Bircher, D.; Tuchscherer, R.; Huizinga, M.; Bayrak, O.; Wood, S.; and Jirsa, J., "Strength and Serviceability Design of Reinforced Concrete Deep Beams," Report No. FHWA/TX-09/0-5253-1, Center for Transportation Research, The University of Texas at Austin, Austin, TX, 2009, 400 pp.
- Wight, J. K., *Reinforced Concrete: Mechanics and Design*, seventh edition, Prentice Hall, Hoboken, NJ, 2015, 1164 pp.
- Reineck, K.-H.; Bentz, E.; Fitik, B.; Kuchma, D. A.; and Bayrak, O., "ACI-DaFStb Databases for Shear Tests on Slender Reinforced Concrete Beams with Stirrups," *ACI Structural Journal*, V. 111, No. 5, Sept.-Oct. 2014, pp. 1147-1156. doi: 10.14359/51686819
- Collins, M. P., and Mitchell, D., "Prestressed Concrete Basics," Canadian Prestressed Concrete Institute, Ottawa, ON, Canada, 1987, 614 pp.
- Vecchio, F. J., and Collins, M. P., "Compression Response of Cracked Reinforced Concrete," *Journal of Structural Engineering*, ASCE, V. 119, No. 12, 1993, pp. 3590-3610. doi: 10.1061/(ASCE)0733-9445(1993)119:12(3590)

## APPENDIX A : DRAWING OF TEST SPECIMEN







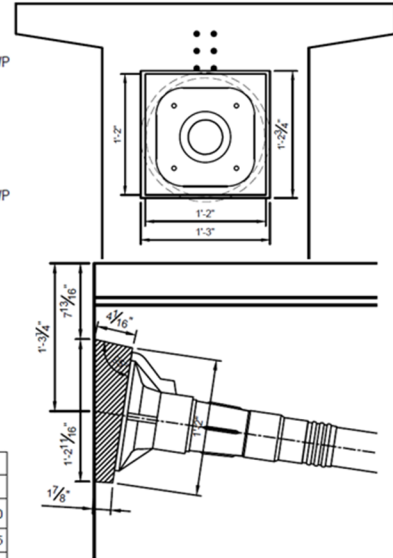
**NOTES:**

1. OTHER REINFORCEMENT AND INSERTS NOT SHOWN FOR CLARITY.
2. PARABOLIC TENDON LAYOUT WILL BE THE SAME FOR P0G, P0U, PSG AND PSU.
3. STRAIGHT TENDON IN THIS DRAWING IS ONLY FOR 0SG AND 0SU

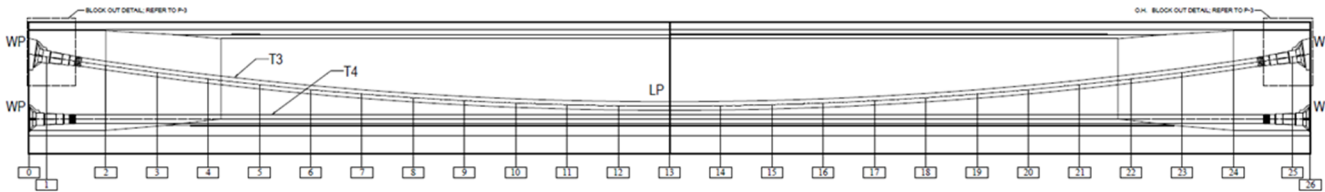
**ELEVATION PT LAYOUT**

TX62-0SG, 0SU (ABOVE), TX62-P0G, P0U (BELOW)

Tendon ID	PROFILE	Node	WP		LP																						AP			
			0	1	1	2	3	4	5	6	7	8	9	10	11	12	13	14	15	16	17	18	19	20	21	22	23	24	25	26
T1	Distance from WP (ft)	0.00	0.68	0.68	3.00	5.00	7.00	9.00	11.00	13.00	15.00	17.00	19.00	21.00	23.00	25.00	27.00	29.00	31.00	33.00	35.00	37.00	39.00	41.00	43.00	45.00	47.00	49.32	50.00	
	Y (in.)	35.25		35.25	35.25	35.25	35.25	35.25	35.25	35.25	35.25	35.25	35.25	35.25	35.25	35.25	35.25	35.25	35.25	35.25	35.25	35.25	35.25	35.25	35.25	35.25	35.25	35.25	35.25	35.25
	Y1 (in.)				33.25	33.25	33.25	33.25	33.25	33.25	33.25	33.25	33.25	33.25	33.25	33.25	33.25	33.25	33.25	33.25	33.25	33.25	33.25	33.25	33.25	33.25	33.25	33.25	33.25	33.25
T2	Distance from WP (ft)	0.00	0.68	0.68	3.00	5.00	7.00	9.00	11.00	13.00	15.00	17.00	19.00	21.00	23.00	25.00	27.00	29.00	31.00	33.00	35.00	37.00	39.00	41.00	43.00	45.00	47.00	49.32	50.00	
	Y (in.)	47.00	45.69		41.47	38.18	35.20	32.54	30.18	28.14	26.42	25.01	23.91	23.13	22.66	22.50	22.66	23.13	23.91	25.01	26.42	28.14	30.18	32.54	35.20	38.18	41.47	45.69	47.00	
	Y1 (in.)				39.47	36.18	33.20	30.54	28.18	26.14	24.43	23.01	21.91	21.13	20.66	20.50	20.66	21.13	21.91	23.01	24.42	26.14	28.18	30.54	33.20	36.18	39.47			



**BLOCK OUT DETAIL**



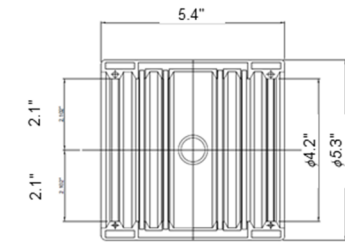
**ELEVATION PT LAYOUT**

TX62-PSG AND PSU

Tendon ID	PROFILE	Node	WP		LP																						AP		
			0	1	1	2	3	4	5	6	7	8	9	10	11	12	13	14	15	16	17	18	19	20	21	22	23	24	25
T3	Distance from WP (ft)	0.00	0.68	0.68	3.00	5.00	7.00	9.00	11.00	13.00	15.00	17.00	19.00	21.00	23.00	25.00	27.00	29.00	31.00	33.00	35.00	37.00	39.00	41.00	43.00	45.00	47.00	49.32	50.00
	Y (in.)	47.00	45.69		41.47	38.18	35.20	32.54	30.18	28.14	26.42	25.01	23.91	23.13	22.66	22.50	22.66	23.13	23.91	25.01	26.42	28.14	30.18	32.54	35.20	38.18	41.47	45.69	47.00
	Y1 (in.)				39.47	36.18	33.20	30.54	28.18	26.14	24.42	23.01	21.91	21.13	20.66	20.50	20.66	21.13	21.91	23.01	24.42	26.14	28.18	30.54	33.20	36.18	39.47		
T4	Distance from WP (ft)	0.00	0.68	0.68	3.00	5.00	7.00	9.00	11.00	13.00	15.00	17.00	19.00	21.00	23.00	25.00	27.00	29.00	31.00	33.00	35.00	37.00	39.00	41.00	43.00	45.00	47.00	49.32	50.00
	Y (in.)	16.40	16.40		16.40	16.40	16.40	16.40	16.40	16.40	16.40	16.40	16.40	16.40	16.40	16.40	16.40	16.40	16.40	16.40	16.40	16.40	16.40	16.40	16.40	16.40	16.40	16.40	16.40
	Y1 (in.)				14.40	14.40	14.40	14.40	14.40	14.40	14.40	14.40	14.40	14.40	14.40	14.40	14.40	14.40	14.40	14.40	14.40	14.40	14.40	14.40	14.40	14.40	14.40	14.40	14.40

**TENDON PROFILE NOTES**

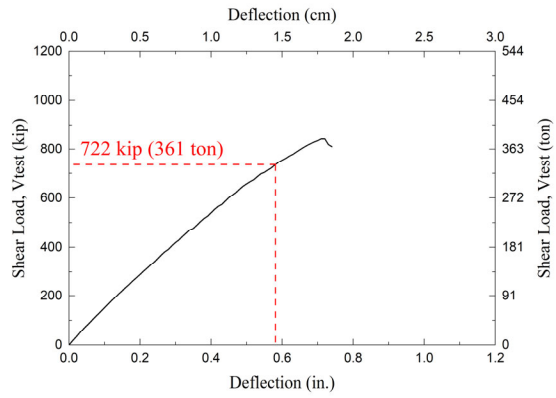
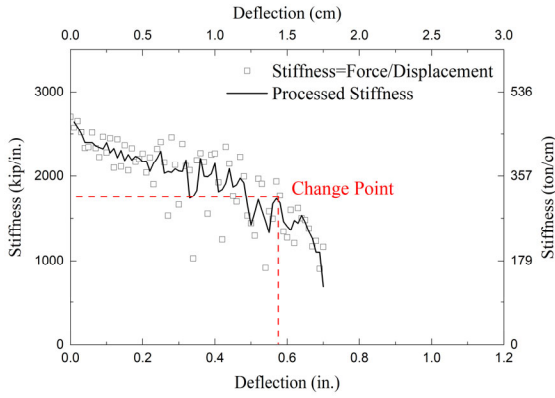
1. WP - WORK POINT
2. AP - ANCHOR POINT
3. LP - LOW POINT
4. Y - VERTICAL DISTANCE OF TENDON MEASURED FROM THE BOTTOM OF GIRDER TO THE CENTER LINE OF DUCT
5. Y1 - SUPPORT HEIGHTS MEASURED FROM THE BOTTOM OF GIRDER TO THE BOTTOM OF THE DUCT
6. DUCT SHOULD BE SUPPORTED EVERY 2 FEET



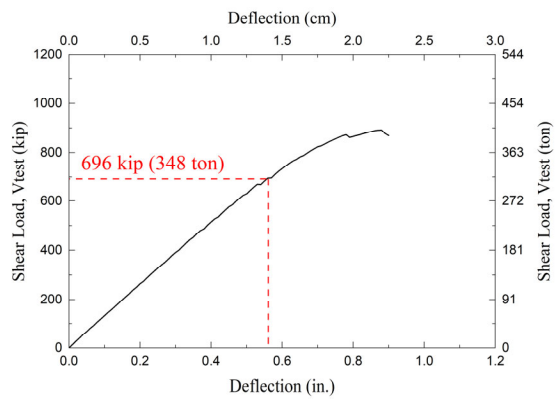
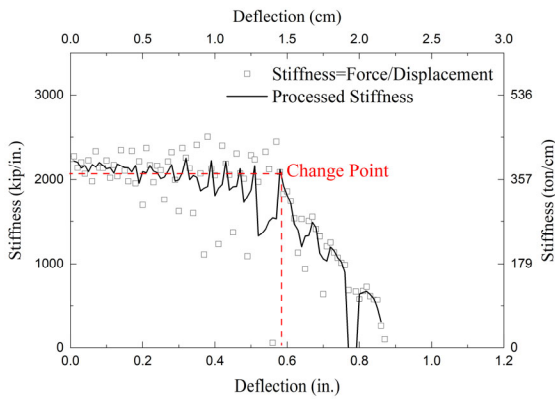
**COUPLER DETAIL**

## **APPENDIX B : STIFFNESS ANALYSIS**

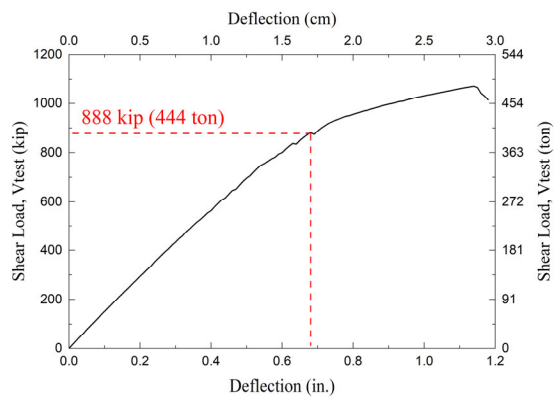
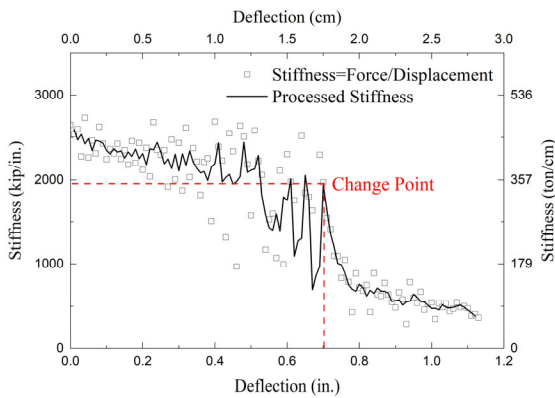
Fig. B1 shows the load-deflection plots along with the stiffness analysis of all tested specimens. The stiffness analysis determined the specimen's change point from linear to nonlinear behavior, calculated by dividing the applied force by the corresponding deflection. This change point matched the onset of a fully developed diagonal shear crack, consistently occurring at load levels of approximately 80% of the ultimate load.



(a) Tx62-0SG (1<sup>st</sup> test)



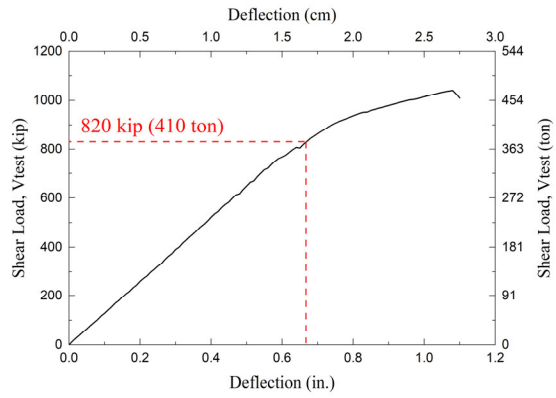
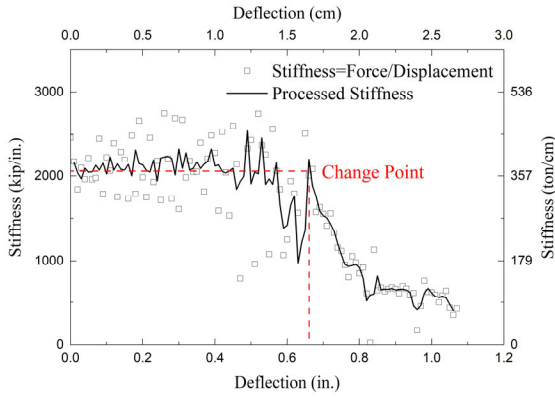
(b) Tx62-0SG (2<sup>nd</sup> test)



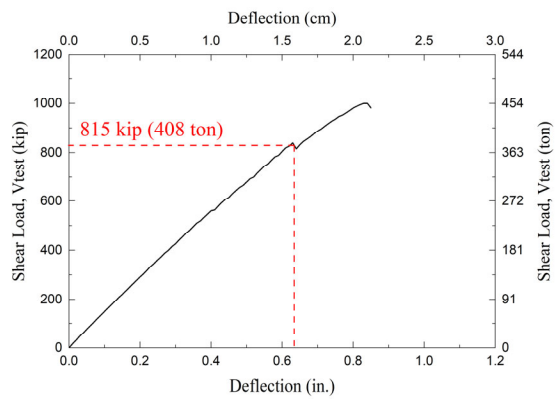
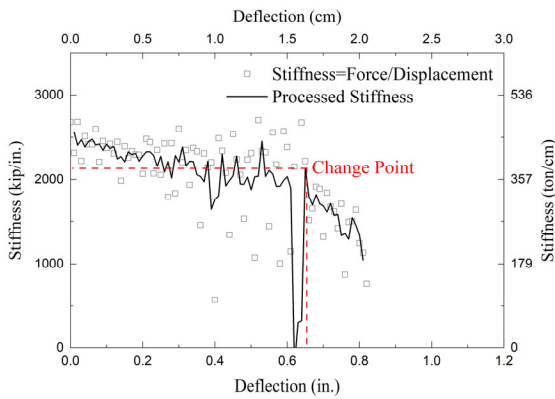
(c) Tx62-P0G (1<sup>st</sup> test)

Fig. B1 – Stiffness analysis to define nonlinear behavior (Left Column) and shear force behavior (Right Column) with respect to deflection

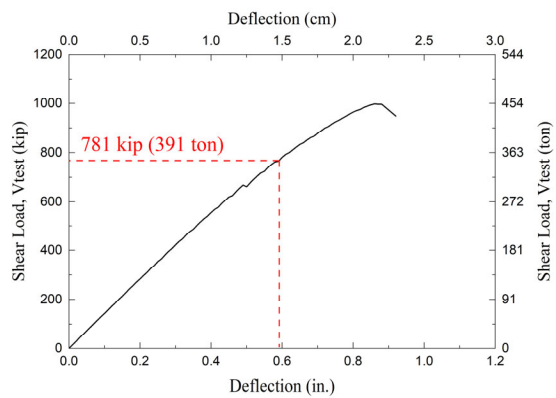
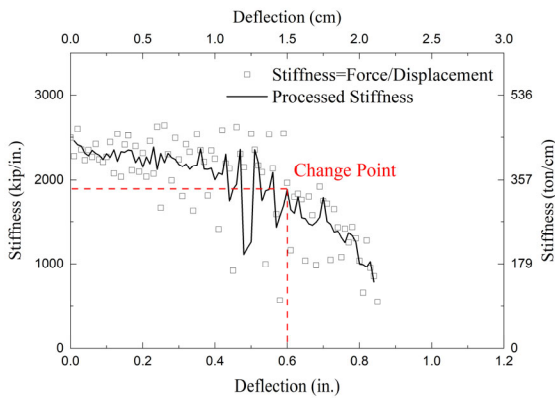




(d) Tx62-P0G (2<sup>nd</sup> test)

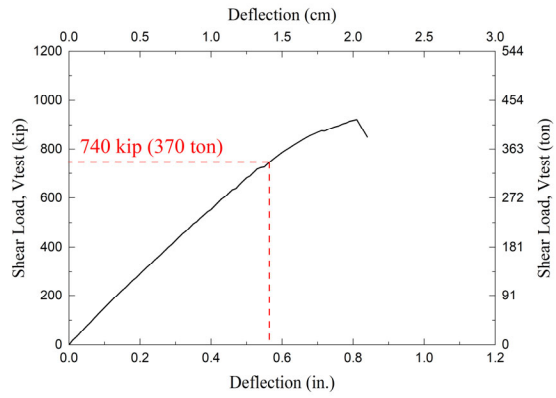
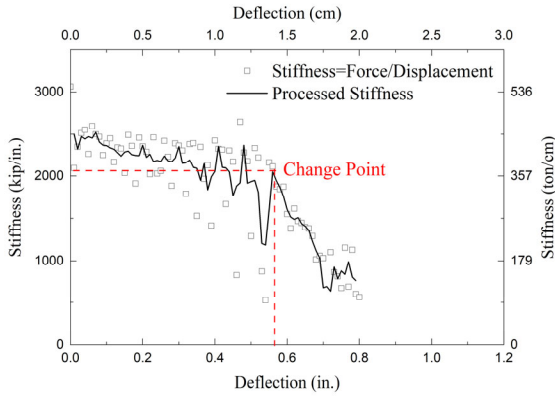


(e) Tx62-PSG (1<sup>st</sup> test)

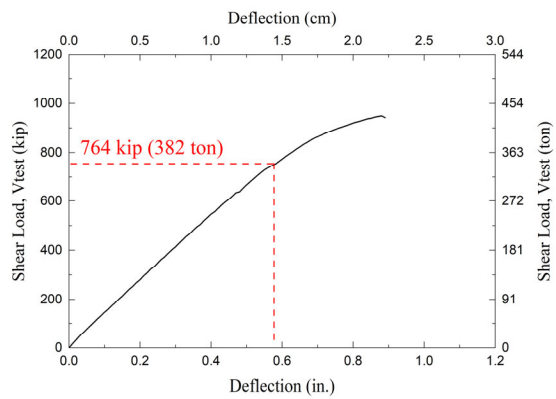
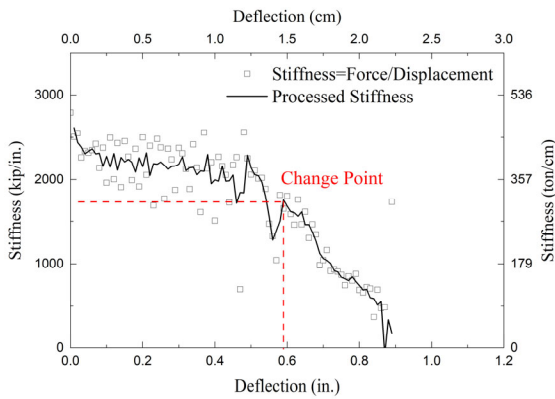


(f) Tx62-PSG (2<sup>nd</sup> test)

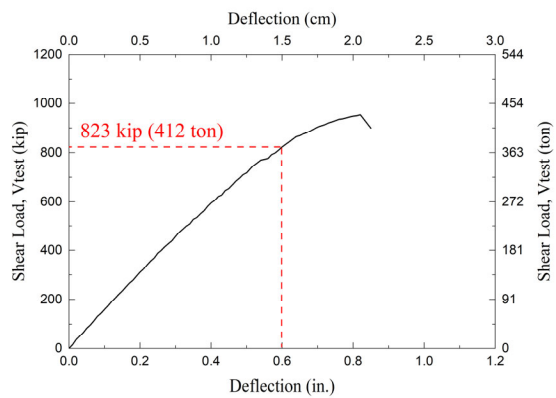
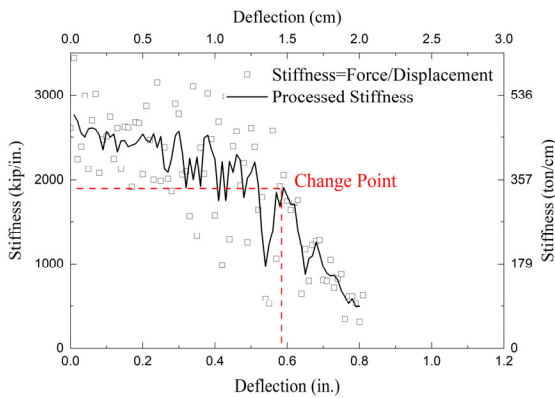
Fig. B1 (cont.) – Stiffness analysis to define nonlinear behavior (left column) and shear force behavior (right column) with respect to deflection



(g) Tx62-0SU (1<sup>st</sup> test)

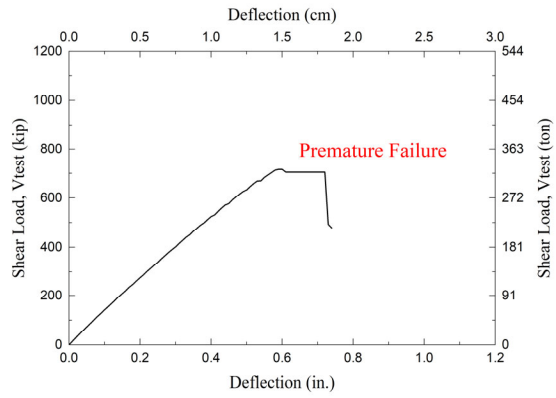
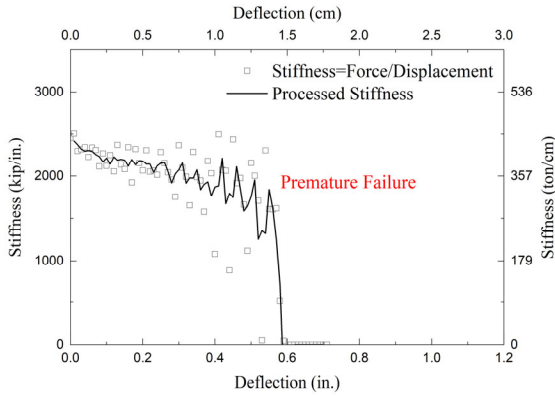


(h) Tx62-0SU (2<sup>nd</sup> test)

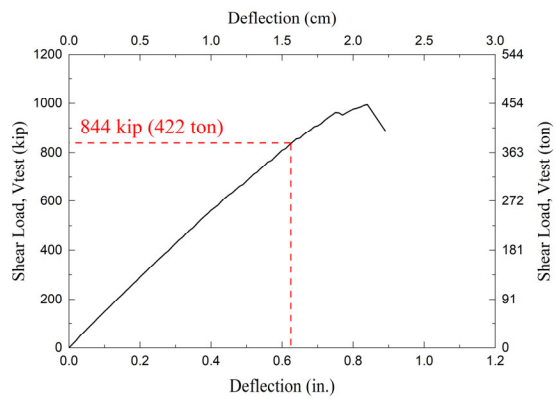
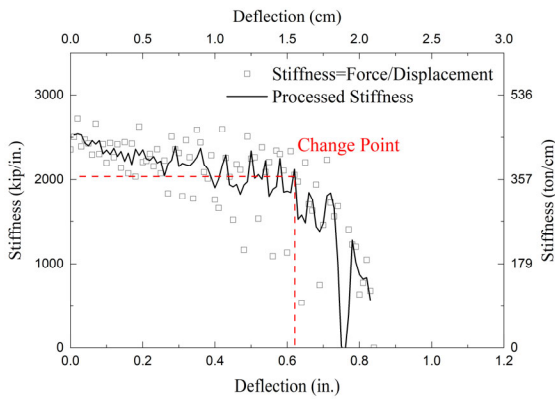


(i) Tx62-P0U (1<sup>st</sup> test)

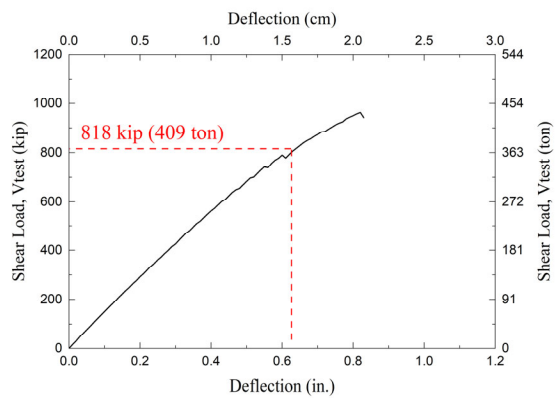
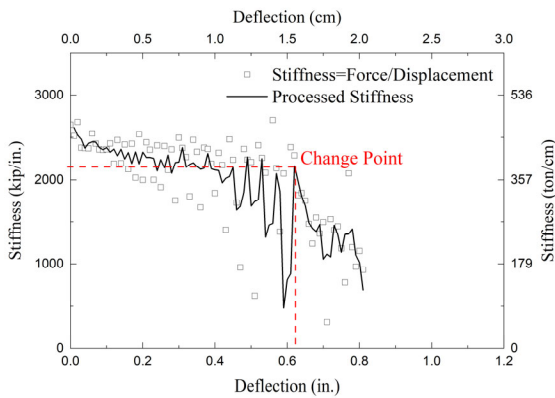
Fig. B1 (cont.) – Stiffness analysis to define nonlinear behavior (left column) and shear force behavior (right column) with respect to deflection



(j) Tx62-P0U (2<sup>nd</sup> test)



(k) Tx62-PSU (1<sup>st</sup> test)



(l) Tx62-PSU (2<sup>nd</sup> test)

Fig. B1 (cont.) – Stiffness analysis to define nonlinear behavior (left column) and shear force behavior (right column) with respect to deflection



**APPENDIX C : DETAILED PROPERTIES OF TEST SPECIMENS**

	Test Specimen	Duct Material	$\phi_{duct}$ , in. (mm)	$b_w$ , in. (mm)	Transverse Reinforcement				Grider $f'_c$ , ksi (MPa)	Grout $f'_c$ , ksi (MPa)
					$\rho_v$ , %	$s_v$ , in. (mm)	$A_v$ , in <sup>2</sup> . (mm <sup>2</sup> )	$f_y$ , ksi (MPa)		
Moore et al. (2015)	Tx62-1(S)	Plastic	3 (76)	7 (178)	0.95	6 (152)	0.40 (258)	67.0 (462)	10.58 (72.9)	5.15 (35.5)
	Tx62-2(S)	Steel	3 (76)	7 (178)	0.95	6 (152)	0.40 (258)	68.3 (471)	11.97 (82.5)	4.28 (29.5)
	Tx62-2(N)	Steel	3 (76)	7 (178)	0.95	6 (152)	0.40 (258)	68.3 (471)	11.97 (82.5)	5.66 (39.0)
	Tx62-3(Ctrl)	Plastic	—	7 (178)	0.95	6 (152)	0.40 (258)	67.4 (465)	11.69 (80.6)	—
	Tx62-4(S)	Steel	3 (76)	7 (178)	1.43	4 (102)	0.40 (258)	66.5 (459)	13.92 (96.0)	9.92 (68.4)
	Tx62-4(N)	Plastic	3 (76)	7 (178)	1.43	4 (102)	0.40 (258)	66.5 (459)	13.61 (93.8)	9.38 (64.7)
	Tx62-5(S)	Plastic	3 (76)	7 (178)	0.32	18 (457)	0.40 (258)	67.4 (465)	12.45 (85.8)	6.33 (43.6)
	Tx62-5(N)	Steel	3 (76)	7 (178)	0.32	18 (457)	0.40 (258)	67.4 (465)	12.45 (85.8)	6.93 (47.8)
	Tx62-6(S)	Plastic	4 (102)	9 (229)	1.15	6 (152)	0.62 (400)	74.4 (513)	12.35 (85.2)	7.92 (54.6)
	Tx62-6(N)	Steel	4 (102)	9 (229)	1.15	6 (152)	0.62 (400)	74.4 (513)	13.16 (90.7)	8.43 (58.1)
	Tx62-7(S)	Steel	3 (76)	9 (229)	1.15	6 (152)	0.62 (400)	75.1 (518)	12.20 (84.1)	7.17 (49.4)
Han et al. (2022)	Tx62-0SG	Plastic	4 (102)	9 (229)	1.15	6 (152)	0.62 (400)	66.7 (460)	10.49 (72.3)	9.05 (62.4)
	Tx62-P0G	Plastic	4 (102)	9 (229)	1.15	6 (152)	0.62 (400)	66.7 (460)	12.21 (84.2)	9.05 (62.4)
	Tx62-PSG	Plastic	4 (102)	9 (229)	1.15	6 (152)	0.62 (400)	66.7 (460)	10.50 (72.4)	9.05 (62.4)
	Tx62-0SU	Plastic	4 (102)	9 (229)	1.15	6 (152)	0.62 (400)	66.7 (460)	11.60 (80.0)	—
	Tx62-P0U	Plastic	4 (102)	9 (229)	1.15	6 (152)	0.62 (400)	66.7 (460)	12.10 (83.4)	—
	Tx62-PSU	Plastic	4 (102)	9 (229)	1.15	6 (152)	0.62 (400)	66.7 (460)	10.84 (73.7)	—